


# Droplet impact on a heated porous plate above the Leidenfrost temperature: A lattice Boltzmann study

**Journal Article****Author(s):**

Wang, Geng; [Fei, Linlin](#) ; Lei, Timan; Wang, Qian; Luo, Kai H.

**Publication date:**

2022-09

**Permanent link:**

<https://doi.org/10.3929/ethz-b-000576057>

**Rights / license:**

[Creative Commons Attribution 4.0 International](#)

**Originally published in:**

Physics of Fluids 34(9), <https://doi.org/10.1063/5.0118079>

# Droplet impact on a heated porous plate above the Leidenfrost temperature: A lattice Boltzmann study

Cite as: Phys. Fluids **34**, 093319 (2022); doi: [10.1063/5.0118079](https://doi.org/10.1063/5.0118079)

Submitted: 3 August 2022 · Accepted: 29 August 2022 ·

Published Online: 26 September 2022





View Online



Export Citation



CrossMark

Geng Wang (王耿),<sup>1</sup> Linlin Fei (费林林),<sup>2</sup>  Timan Lei (雷体蔓),<sup>1</sup> Qian Wang (王倩),<sup>3</sup> and Kai H. Luo (罗开红)<sup>1,a)</sup> 

## AFFILIATIONS

<sup>1</sup>Department of Mechanical Engineering, University College London, Torrington Place, London WC1E 7JE, United Kingdom

<sup>2</sup>Chair of Building Physics, Department of Mechanical and Process Engineering, ETH Zürich (Swiss Federal Institute of Technology in Zürich), Zürich 8092, Switzerland

<sup>3</sup>School of Mechanical Engineering, Shanghai Jiao Tong University, Shanghai 200240, China

<sup>a)</sup>Author to whom correspondence should be addressed: [k.luo@ucl.ac.uk](mailto:k.luo@ucl.ac.uk)

## ABSTRACT

In the past few decades, the droplet impact on a heated plate above the Leidenfrost temperature has attracted immense research interest. The strong hydrophobicity caused by the Leidenfrost effect leads to the droplet bouncing from a flat plate at a given contact time predicted by the classical Rayleigh theory. Numerous investigations were conducted to break the theoretical Rayleigh's limit to reduce the interfacial contact time. Recently, a droplet was observed to form a pancake shape and bounce as it impacted nanotube or micropost surfaces above the Leidenfrost temperature. This led to a significant reduction in droplet contact time. However, this unique bouncing phenomenon is still not fully understood, such as the influence of the plate configuration and the relationship between the droplet rebound time and evaporation mass loss. In this study, we carry out a numerical study of the droplet impact dynamics on a heated porous plate above the Leidenfrost temperature, using a multiphase thermal lattice Boltzmann model. Our model is constructed within the unified lattice Boltzmann method framework and is first validated based on theoretical and experimental results. Then, a comprehensive parametric study is performed to investigate the effects of the impact Weber number, the plate temperature, and the plate configurations on the droplet bouncing dynamics. Results show that higher plate temperature, larger Weber number, and smaller pore intervals can accelerate the droplet rebound and promote the droplet pancake bouncing. We demonstrate that the occurrence of the pancake bouncing is attributed to the additional lift force provided by the vapor pressure due to the evaporation of liquid inside the pores. Moreover, the droplet maximum spreading time and maximum spreading factor can be described by a power law function of the impact Weber number. The droplet evaporation mass loss increases linearly with the impingement Weber number and the plate opening fractions. This study provides new insights into the Leidenfrost droplet impingement on porous plates, which may potentially facilitate the design of novel engineering surfaces and devices.

© 2022 Author(s). All article content, except where otherwise noted, is licensed under a Creative Commons Attribution (CC BY) license (<http://creativecommons.org/licenses/by/4.0/>). <https://doi.org/10.1063/5.0118079>

## I. INTRODUCTION

Droplet impingement on a heated plate is ubiquitous in nature and the industry such as aviation, power generation, and process engineering.<sup>1,2</sup> Recently, the rapid development of miniaturized electronic devices creates an urgent need for innovative cooling approaches, such as spray cooling, which requires optimized manipulation of droplet dynamics on a heated plate.<sup>3</sup> This demands detailed insights into the effects of the plate temperature, plate geometry, and liquid properties on droplet impact dynamics and its evaporation over the heated plate.<sup>4–6</sup> According to the classical boiling heat transfer theory, the

droplet experiences several heating regimes when the plate temperature is increased, for example, the nucleate boiling regime, the transition boiling regime, and the film boiling regime.<sup>1,7</sup> Remarkably, in the film boiling regime, the plate temperature is above the Leidenfrost point and the droplet's lower surface evaporates rapidly. As a result, a thin vapor layer is generated between the liquid phase and the solid plate, impeding the contact of the droplet with the plate. The Leidenfrost droplet, thus, demonstrates similar dynamics as its impingement on superhydrophobic surfaces.<sup>4</sup> For example, it has been observed that a droplet rebounds after impacting a hot plate above the

Leidenfrost temperature. On a flat plate, the contact time ( $t_c$ ) of the droplet approximately follows Rayleigh's theory, where  $t_c/\tau = \pi/4$  [ $\tau = (D_0^3 \rho_l/\sigma)^{0.5}$  is the inertia-capillarity time].<sup>4,8–10</sup> Also, the vapor layer between the droplet and the heated plate prevents heat transfer and droplet evaporation, which minimizes the heat flux at the Leidenfrost point.<sup>1,7</sup> Considering that the solid–liquid interface contact time is critical to applications such as anti-icing, spray cooling, and heat transfer, the study of droplet impingement dynamics on superhydrophobic surfaces<sup>11,12</sup> and heated surfaces<sup>4</sup> has attracted increasing interest in the past few decades.

Considerable efforts have been made to experimentally explore the Leidenfrost droplet dynamics. Recent advances can be generally divided into three families: (1) understanding of the Leidenfrost droplet hydrodynamics. Lagubeau *et al.*<sup>13</sup> first observed the self-propelled characteristics of the Leidenfrost droplet on a ratchet surface, which was attributed to the interaction of the vapor flow and asymmetric textures. In 2018, Bouillant *et al.*<sup>14</sup> found that the Leidenfrost droplet also demonstrated self-propelled characteristics on a hot flat plate. More recently, an interesting self-bouncing mechanism was observed for a deposited Leidenfrost droplet on a hot surface.<sup>15</sup> (2) Controlling of the Leidenfrost point to benefit the heat transfer. Celestini *et al.*<sup>16</sup> found that the Leidenfrost point could drop to room temperature as the ambient pressure decreased. Kwon *et al.*<sup>17</sup> and Kruse *et al.*<sup>18</sup> suggested that the Leidenfrost point was increased for any droplet in sparse hot texture surfaces. Arnaldo Del Cerro *et al.*<sup>19</sup> observed that the microholes array surfaces can decrease the Leidenfrost point. More recently, Jiang *et al.*<sup>20</sup> inhibited the Leidenfrost point to over 1000 °C by designing the steel pillar surfaces with an insulating membrane. (3) Reducing the droplet contact time to break the limitation of Rayleigh's theory. Liu *et al.*<sup>21</sup> observed an explosive pancake bounce as the Leidenfrost droplet impacts a surface with a micro-scale micropore or micropost arrays, which significantly decreased the droplet contact time. Similar explosive pancake bouncing and contact time decreasing phenomena were observed when the Leidenfrost droplet impinged on a surface with nanotubes.<sup>22,23</sup> In addition, the explosive bounce has been observed for a multicomponent<sup>24</sup> droplet or a contaminated droplet<sup>25</sup> impacting a heated plate over the Leidenfrost temperature.

In addition to experimental studies, with the rapid development of computer technologies in recent decades, numerical methods are being increasingly adopted to study the Leidenfrost droplet dynamics. Compared with traditional experimental methods, numerical methods have the advantages of precise control of the physical parameters, convenience to obtain quantitative data, and ease to change the experimental configurations. Some early studies used the volume of fluid (VOF) algorithm to simulate the droplet impact on a flat surface (FS) above the Leidenfrost temperature.<sup>26–28</sup> However, it is still challenging to couple the traditional “interface tracking” multiphase model with the phase change model. Some studies introduced a virtual vapor layer with a pressure-dependent model<sup>26</sup> or a one-dimensional model<sup>27,28</sup> to prevent direct contact of the droplet with the hot plate. More recently, Chakraborty *et al.*<sup>29</sup> developed a lubrication model to predict the fluid flow inside the vapor layer of Leidenfrost drops.

Nevertheless, the capture of the vapor layer in most previous numerical studies depends on artificial models. Alternatively, the lattice Boltzmann method (LBM) provides a promising approach to model this complex phase change problem. Benefitting from its mesoscopic nature, the LBM is capable of incorporating realistic physical models of

interfacial and phase change problems.<sup>30,31</sup> In the pseudopotential LBM, for example, a realistic equation of state (EOS) of the fluid can be introduced to deal with the temperature-dependent phase change.<sup>32,33</sup> Remarkably, Li *et al.*<sup>34</sup> adopted a multiple-relaxation-time (MRT) pseudopotential LB model to simulate a Leidenfrost droplet self-propelled on ratchet surfaces. Both Xu *et al.*<sup>35</sup> and Karami *et al.*<sup>36</sup> conducted systematic parametric studies for a two-dimensional (2D) droplet impacting a heat plate over the Leidenfrost point by using MRT LBM. Recently, Xu *et al.*<sup>37</sup> adopted a three-dimensional cascaded lattice Boltzmann method (CLBM) model proposed by Fei *et al.*<sup>38</sup> to simulate droplet impact on heated micropillar surfaces, which has reproduced the droplet impingement dynamics for a wide range of temperatures successfully.

Although many efforts have been devoted to exploring the Leidenfrost droplet dynamics on a flat plate, there have been no systematic investigations into the Leidenfrost droplet impact on a heated porous plate with pore sizes ranging from nanometer to micrometer, let alone explanations for the complex physics at play. For this problem, the traditional experimental techniques face significant challenges in the precise control of the plate temperature, impact velocity, and pore size.<sup>21</sup> It is also difficult to obtain quantitative data (such as the quality of evaporated liquid) and observe the fluid flow inside the pores. Therefore, it is critical to conduct a systematic numerical investigation of this problem. In this study, we adopt the unified lattice Boltzmann method (ULBM) with the entropic-multi-relaxation-time (KBC, proposed by Karlin, Boschj, and Chikatamarla) collision operator combined with the phase-change pseudopotential multiphase model<sup>39</sup> to numerically study a droplet impacting on a heated porous plate above the Leidenfrost temperature. A comprehensive parametric study is conducted by changing the droplet impact Weber number ( $We$ ), the plate temperature, and the plate configurations, which aims to gain further physical insights into the mechanisms of this complex droplet dynamics through both qualitative and quantitative analyses. In Sec. II, we provide a brief introduction to the LB models, followed by model validation against previous theoretical, numerical, and experimental results. In Sec. III, we conduct a detailed investigation into the influence of the impact of the Weber number on various plate temperatures and geometries. Additionally, the effects of pore intervals are scrutinized. Finally, conclusions are drawn in Sec. IV.

## II. METHODOLOGY

### A. UCLBM (KBC) model for multiphase flow

In this section, we briefly introduce the LB method, which is used in this study. The mesoscopic evolution equation of the ULBM in central moment space can be written as<sup>39</sup>

$$\begin{aligned} f_i(\mathbf{x} + \mathbf{e}_i \Delta t, t + \Delta t) \\ \equiv f_i^*(\mathbf{x}, t) = \mathbf{M}^{-1} \mathbf{N}^{-1} (\mathbf{I} - \mathbf{S}) |\tilde{T}_i\rangle + \mathbf{M}^{-1} \mathbf{N}^{-1} \mathbf{S} |\tilde{T}_i^{eq}\rangle \\ + \mathbf{M}^{-1} \mathbf{N}^{-1} (\mathbf{I} - \mathbf{S}/2) |C_i\rangle, \end{aligned} \quad (1)$$

where  $i$  indexes the 19 discrete velocity set,  $f_i$  and  $f_i^*$  are the pre-collision and post-collision distribution functions, respectively.  $\mathbf{I}$ ,  $\mathbf{M}$ ,  $\mathbf{N}$ , and  $\mathbf{S}$  are the unit matrix, transformation matrix, shift matrix, and relaxation matrix, respectively.  $|\tilde{T}_i\rangle$  is the moment set in the co-moving framework and superscript  $eq$  represents the equilibrium state.  $|C_i\rangle$  is the discrete forcing term, which includes the total force acting

on the system. In this study, a consistent forcing scheme in central moment space proposed by Fei *et al.*<sup>40</sup> is adopted,

$$|C_i\rangle = [0, F_x, F_y, F_z, 0, 0, 0, 0, 0, 0, F_x C_s^2, F_x C_s^2, F_y C_s^2, F_z C_s^2, F_y C_s^2, F_z C_s^2, 0, 0, 0]^T. \quad (2)$$

The explicit expressions of matrix  $\mathbf{M}, \mathbf{N}, \mathbf{M}^{-1}, \mathbf{N}^{-1}$ , as well as the moment sets  $|\tilde{T}_i\rangle$  and  $|\tilde{T}^{eq}\rangle$ , are given in Ref. 39. It has been comprehensively proven that the ULBM framework has the ease to incorporate improved LB schemes<sup>41</sup> and excellent portability across different lattice models.<sup>40,42</sup> The KBC entropic operator<sup>43</sup> is implemented by introducing the entropic stabilizer into the higher-order relaxation parameters; hence, the relaxation matrix  $\mathbf{S}$  can be written as

$$\mathbf{S} = \text{diag}(0, 1, 1, 1, s_v, s_v, s_v, s_v, s_v, s_v, s_v, s_v, s_v, s_v, s_v, s_v, s_v, s_v, s_v), \quad (3)$$

where  $1/s_v = \nu/(C_s^2 \Delta t) + 0.5$  depends on the liquid kinematic viscosity. The entropic stabilizer  $\gamma$  is calculated by

$$\gamma = \frac{1}{s_v} - \left(1 - \frac{1}{s_v}\right) \frac{\sum_i \frac{\Delta s_i \Delta h_i}{f_i^{eq}}}{\sum_i \frac{\Delta h_i \Delta h_i}{f_i^{eq}}}, \quad (4)$$

where  $s_i$  and  $h_i$  are the shear part and high order part of the distribution function, respectively.  $\Delta s_i = s_i - s_i^{eq}$  and  $\Delta h_i = h_i - h_i^{eq}$  are the deviations. The ULBM with the KBC operator has been shown to dramatically reduce spurious velocities.<sup>39</sup> More details about the ULBM (KBC) model can be found in Refs. 39 and 41.

For the multiphase flow simulation, the combined pseudopotential model<sup>44</sup> is employed to describe the interaction force among different phases, which is

$$\mathbf{F}_{int} = -0.5AG \sum_i w(|e_i|^2) \psi^2(\mathbf{x} + \mathbf{e}_i) \mathbf{e}_i - (1 - A)G\psi(\mathbf{x}) \sum_i w(|e_i|^2) \psi(\mathbf{x} + \mathbf{e}_i) \mathbf{e}_i, \quad (5)$$

where  $A$  is a tunable parameter, which can be used to adjust the thermodynamic consistency,  $G = -1$  is the interaction strength, and  $w(|e_i|^2)$  are the weights for the D3Q19 lattice model.  $\psi$  is the square-root-form pseudopotential,<sup>45</sup>

$$\psi = \sqrt{\frac{2(P_{EOS} - \rho c_s^2)}{Gc^2}}, \quad (6)$$

where  $c = 1$  is the lattice constant,  $c_s^2 = 1/3$  is the lattice sound speed, and  $P_{EOS}$  is the pressure calculated by the equation of state (EOS). In this work, in order to simulate the multiphase flow with phase change phenomena, we use the Peng–Robinson EOS, which can be written as

$$P_{EOS} = \frac{\rho RT}{1 - b\rho} - \frac{a\varphi(T)\rho^2}{1 + 2b\rho - b^2\rho^2}, \quad (7)$$

where  $a = 0.4572R^2 T_c^2 / P_c$ ,  $b = 0.0778RT_c / P_c$ , and  $\varphi(T) = [1 + (0.37464 + 1.54226\omega - 0.26992\omega^2)(1 - \sqrt{T/T_c})]^2$ , and  $P_c$  and  $T_c$  stand for the critical pressure and critical temperature, respectively. In the following simulations, without specifying, we set  $R = 1$ ,  $\omega = 0.344$ ,  $a = 1/76$ , and  $b = 2/21$ , with the corresponding  $T_c = 0.02351$  and  $P_c = 0.0192$ .

In addition, when simulating the Leidenfrost droplet impingement, the gas phase and liquid phase are driven by the buoyancy force,

$$\mathbf{F}_b = -(\rho - \rho_{avg})g\mathbf{j}, \quad (8)$$

where  $\rho_{avg}$  is the average density of the liquid and vapor phases. The total force acting on the fluid is  $\mathbf{F} = \mathbf{F}_b + \mathbf{F}_{int}$ . The improved virtual-density scheme proposed by Li *et al.*<sup>46</sup> is employed to treat the interaction between the solid phase and liquid phase. The virtual density of the bounded layer in the solid phase can be described as

$$\rho_w(\mathbf{x}) = \frac{\sum_i w(|e_i|^2) \rho(\mathbf{x} + \mathbf{e}_i \Delta t) s(\mathbf{x} + \mathbf{e}_i \Delta t)}{\sum_i w(|e_i|^2) s(\mathbf{x} + \mathbf{e}_i \Delta t)}, \quad (9)$$

where  $s(\mathbf{x})$  is an indicator function, which is equal to 0 for the solid phase and 1 for the fluid phase, respectively. Based on this setup, the interaction force between the solid phase and liquid phase can be calculated by Eq. (5), and the droplet static contact angle under the isothermal condition equals  $90^\circ$ . It should be mentioned that the above multiphase ULBM (KBC) model has been verified by existing experiments of droplet dynamics. More details can be found in our recent work.<sup>39</sup>

Inspired by Li *et al.*,<sup>47</sup> the temperature field for the liquid–vapor phase-change can be written as

$$\frac{\partial T}{\partial t} = -\mathbf{u} \cdot \nabla T + \frac{1}{\rho c_v} (\lambda \nabla^2 T + \nabla \lambda \cdot \nabla T) - \frac{T}{\rho c_v} \left( \frac{\partial P_{EOS}}{\partial T} \right)_\rho \nabla \cdot \mathbf{u}, \quad (10)$$

where  $\lambda$  is the thermal conductivity and  $c_v$  is the specific heat capacity at constant volume. Following the work of Li *et al.*,<sup>47</sup> we use the finite difference method to solve the above temperature equation, and the time discretization is realized using the fourth-order Runge–Kutta scheme,

$$\begin{aligned} T^{t+\Delta t} &= T^t + \frac{\Delta t}{6} (h_1 + 2h_2 + 2h_3 + h_4), \\ h_1 &= K(T^t), \quad h_2 = K\left(T^t + \frac{\Delta t}{2} h_1\right), \\ h_3 &= K\left(T^t + \frac{\Delta t}{2} h_2\right), \quad h_4 = K(T^t + \Delta t h_3), \end{aligned} \quad (11)$$

where  $K(T)$  denotes the right-hand side of Eq. (10). The coupling of the temperature field and the liquid–vapor phase change is achieved through the EOS of the fluid [Eq. (7)]. It is worth mentioning that the phase change multiphase model presented above has been incorporated into the ULBM (with cascaded lattice Boltzmann model) to simulate the three-dimensional pool boiling.<sup>38,41</sup>

## B. Verification of the multiphase thermal LB model

We first validate the thermodynamic consistency of the adopted multiphase model. We simulate a flat surface and change the system temperature from  $0.5 T_c$  to  $0.9 T_c$ , keeping the tunable parameter  $A$  in Eq. (5) at  $-0.88$ . We compare the simulated coexistence densities of the gas phase and the vapor phase with the Maxwell equal-area rules. As presented in Fig. 1, the simulated coexistence densities (triangle symbols) coincide with the Maxwell construction results (lines) for a

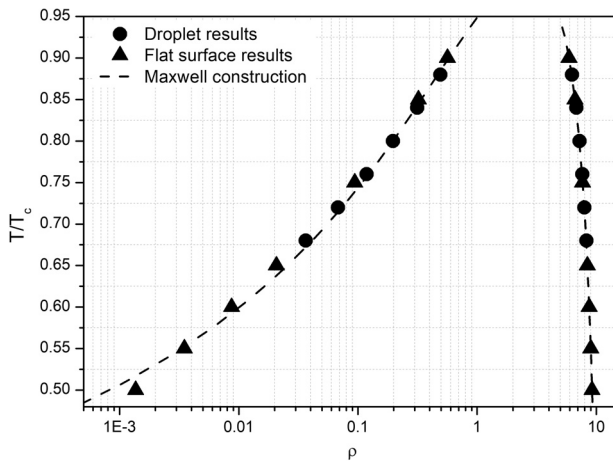


FIG. 1. Comparison of the simulated coexistence densities (symbols) and the Maxwell construction law (lines) for different reduced temperatures.

wide range of temperatures and density ratios (up to 6700), which proves the good thermodynamic consistency of our numerical model. We also simulate a static droplet with the initial radius  $R_0 = 50$  lattices located at the center of a  $4R_0 \times 4R_0 \times 4R_0$  box, with the periodic boundaries in all directions. The density profile can be described by the following function:

$$\rho(r) = \frac{\rho_l + \rho_g}{2} + \frac{\rho_l - \rho_g}{2} \tanh\left[\frac{2(r - R_0)}{W}\right], \quad (12)$$

where  $W = 4$  is the approximate interface thickness by adopting the introduced setup in Sec. II A, and  $r$  represents the distance to the droplet center.  $\rho_l$  and  $\rho_g$  are coexistence densities in the gas phase and vapor phase, respectively.  $A$  is set as  $-0.84$  and the system temperatures are varied from  $0.68 T_c$  to  $0.88 T_c$ , while all the other parameters kept the same. As indicated in the figure, the simulated coexistence

densities for the droplet test (circle symbols) are also consistent with the Maxwell construction results. Importantly, the maximum spurious velocities are lower than  $0.0025$  for all simulations due to the use of the ULBM (KBC) collision operator.

Further verification of the model considering the temperature field is conducted by simulating the evaporation of a single droplet. We simulate a liquid cylinder (equivalent to a 2D droplet) with an initial diameter  $D_0 = 70$ , evaporating in a temperature gradient. The simulation domain is set as  $200 \times 200 \times 1$  with periodic boundaries in all directions. To compare with the results in Ref. 38, we set the temperature of the liquid phase as  $0.86 T_c$  and the surrounding vapor temperature as  $T_c$ , with  $a = 2/49$  and  $b = 2/21$  in the EOS. The kinematic viscosities and the specific heat capacities of the liquid phase and the gas phase are set as the same, e.g.,  $c_{v_l} = c_{v_g} = 6$ ,  $\nu_l = \nu_g = 0.1$ .

The results of the current study (symbols) are compared with the previous simulation results by Fei *et al.* (lines)<sup>38</sup> and  $D^2$  law. To this end, the results are plotted as a  $(D/D_0)^2$  vs  $t^*$  in Fig. 2(a), where the non-dimensional time  $t^* = T\nu_g/D_0^2$ . As shown in the figure, our simulation results are in exact agreement with the previous simulation results for two different thermal conductivities,  $\lambda_l = \lambda_g = 1/3$  and  $\lambda_l = \lambda_g = 2/3$ . Also, the temperature distribution and velocity vectors around the evaporating droplet are shown in Fig. 2(b), demonstrating that the liquid phase evaporation is driven by the temperature gradient. The quantitative and qualitative results prove the accuracy of the model implementation for thermal multiphase flows.

### C. Validation via Leidenfrost droplet impact on a flat plate

Model validation is conducted via simulating droplet impact on a heated plate above the Leidenfrost temperature. In the following simulations, unless otherwise stated, the initial droplet radius is set as  $R_0 = 50$ . The liquid and vapor saturated temperature ( $T_s$ ) is kept as  $0.8 T_c$ , which leads to the corresponding coexistence densities at  $\rho_l = 7.2$  and  $\rho_v = 0.197$ . By using this setup, the measured surface

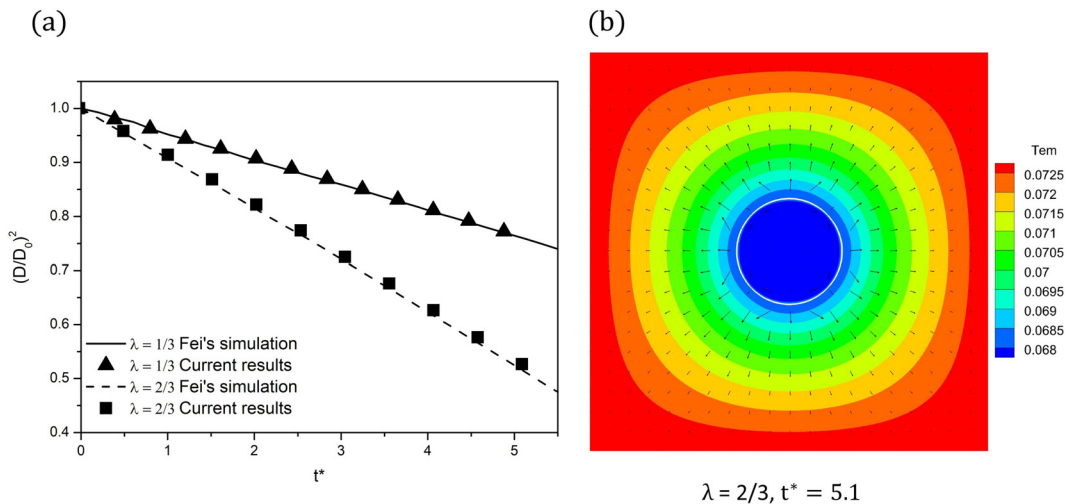


FIG. 2. (a) Comparison of the evolution of  $(D/D_0)^2$  for current simulation results (solid symbols) and previous simulation results (lines), for two different thermal conductivities,  $\lambda_l = \lambda_g = 1/3$  and  $\lambda_l = \lambda_g = 2/3$ . (b) The temperature distribution and velocity vectors around the evaporating droplet (white profile).

**TABLE I.** Experiment configurations and our simulation setups for the validation cases.

Case	Experiment conditions					Simulation parameters				
	$Pr_g$	$Pr_l$	$Ja$	$We$	$Bo$	$Pr_g$	$Pr_l$	$Ja$	$We$	$Bo$
1	0.76	1.57	0.48	2.1	0.18	0.94	1.49	0.53	2.1	0.14
2	0.76	1.57	0.51	16.3	0.23	0.94	1.49	0.61	16.0	0.19
3	0.76	1.57	0.34	22.8	0.18	0.94	1.49	0.50	21.6	0.16

tension ( $\sigma$ ) is 0.112 35. According to Ref. 38, the latent heat ( $h_{fg}$ ) of the droplet is calculated by

$$h_{fg} = h_g - h_l = \int_{\rho_g}^{\rho_l} \frac{1}{\rho^2} \left[ T \left( \frac{\partial P_{EOS}}{\partial T} \right)_\rho - P_{EOS} \right] d\rho + \frac{P_{EOS}}{\rho_g} - \frac{P_{EOS}}{\rho_l}, \quad (13)$$

where  $h_g$  and  $h_l$  are the enthalpy values of the gas and liquid phases, respectively. Substituting the Peng–Robinson EOS in Sec. II A into Eq. (13), the corresponding  $h_{fg}$  equals to 0.1416. In addition, we set the liquid kinematic viscosity ( $\nu_l$ ) as 0.007 so that the Ohnesorge number is  $Oh = (\rho_l \nu_l) / \sqrt{D_0 \rho_l \sigma} = 0.0056 < 0.01$ , which implies the influence of the viscous force can be ignored compared with the inertial force and surface tension.<sup>48</sup> The kinematic viscosity ratio  $\nu_g / \nu_l$  between the gas phase and liquid phase is set as 20, which is comparable to the realistic condition.

To get an accurate prediction of the heat transfer and phase change process, we set the Prandtl number (the ratio of the momentum diffusivity to the thermal diffusivity) of the liquid phase ( $Pr_l = \nu_l \rho_l c_{v_l} / \lambda_l$ ), Prandtl number of the gas phase ( $Pr_g = \nu_g \rho_g c_{v_g} / \lambda_g$ ), and Jacob number  $Ja = c_{v_l} (T_h - T_s) / h_{fg}$  (the ratio of the sensible heat to the latent heat during the phase change) comparable to the realistic conditions, with the thermal properties of the liquid and vapor phases referring to the values of the saturated state. In addition, the Weber number ( $We = D_0 \rho_l U^2 / \sigma$ , representing the ratio of the inertial force to the capillary force, where  $U$  is the droplet initial velocity) and Bond number ( $Bo = \rho_l g D_0^2 / \sigma$ , standing for the gravity compared to the surface tension, which is usually used to evaluate the influence of gravity) are also chosen to represent the experimental conditions. Based on the above setup, the corresponding fluid properties (e.g.,  $c_v$  and  $\lambda$ ) and operating parameters (e.g.,  $U$  and  $g$ ) in the lattice unit can be

determined. For the following cases, we set  $c_{v_l} = 7.4$ ,  $c_{v_g} = 3.4$ ,  $\lambda_l = 0.25$ ,  $\lambda_g = 0.1$ , which leads to  $Pr_g = 0.94$  and  $Pr_l = 1.49$ , respectively. Remarkably, the following interpolation form is used to calculate the fluid properties at the liquid–gas interface:

$$X = X_g + (X_l - X_g) \frac{\rho - \rho_g}{\rho_l - \rho_g}, \quad (14)$$

where  $X$  stands for the corresponding fluid properties.

It is worth mentioning that the conversion of a variable  $\Gamma$  from lattice (with subscript  $l$ ) to physical units (with subscript  $p$ ) is based on the characteristic variable ( $\Gamma_m$ ), which can be written as  $\Gamma_p = (\Gamma_{m,p} / \Gamma_{m,l}) \Gamma_l$ . For example, we choose the droplet diameter  $D_0$  as the characteristic length; thus, the physical length can be calculated by  $L_p = (D_{0,p} / D_{0,l}) L_l$ . Regarding the calculation of the droplet initial velocity in lattice unit ( $U_l$ ), it is based on the dimensionless Weber number, e.g.,  $U_l = \sqrt{\sigma We / \rho_l D_{0,l}}$ . Additionally, the conversion from the simulation step ( $t_l$ ) into the physical time ( $t_p$ ) is based on the dimensionless time, where  $t_p U_p / D_{0,p} = t_l U_l / D_{0,l}$ .

Similar to Refs. 36 and 37, when simulating the Leidenfrost droplet impingement, the top wall of the simulation domain is set as the outflow boundary. The solid phase and bottom wall are set as the non-slip boundaries with the constant temperature  $T_h$ . The side walls of the simulation domain are set as the periodic boundaries. As pointed in Ref. 6, for most cases of droplet impact on a high temperature plate, the contact temperature between the droplet and the plate reaches the wall temperature immediately after the initial droplet contact. Consequently, we set the temperature of the fluid at the first layer near the solid wall as the wall temperature ( $T_h$ ). Three cases with different impacting velocities and plate temperatures are simulated, and the experiment conditions and simulation setups of the corresponding cases are shown in Table I.

The first case is to simulate the experiment in Ref. 49, where a water droplet with the initial diameter ( $D_0$ ) of 2.05 mm impacts on a 385 °C plate with a velocity  $U = 0.24$  m/s. The simulation results for case 1 are shown in Fig. 3 (bottom column). It can be seen that after the droplet impacts the heated plate, it spreads in the horizontal direction. A very thin vapor film can be observed at the bottom of the droplet, which is generated by the evaporation of the contact liquid. Then, during the recoiling stage of the droplet, the levitated droplet re-contacted with the bottom wall. Finally, the droplet completely rebounds off from the plate, owing to the strong hydrophobic characteristics caused by the Leidenfrost effect. It can be observed that the

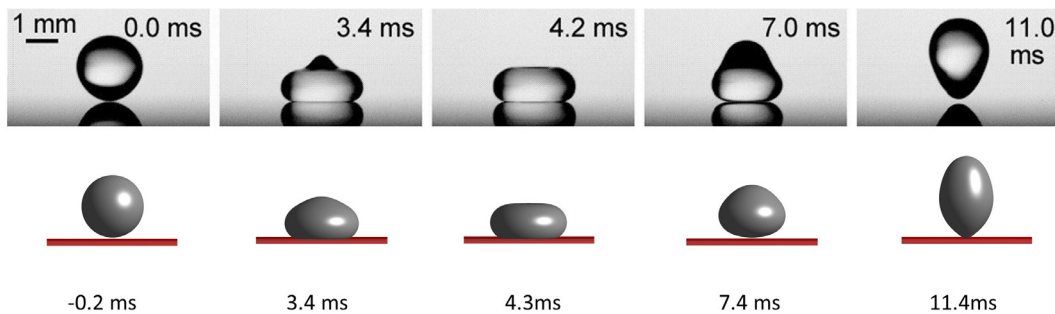


**FIG. 3.** Experiment snapshots (top column) and simulation results (bottom column) of a droplet impacting an overheated flat plate with  $We = 2.1$ ,  $Ja = 0.53$ .

simulation results agreed well with the experiment snapshots (top column) qualitatively.

We then simulate Leidenfrost droplet impact on an overheated plate with a higher Weber number (case 2 in Table I). In the original experiment by Wachters *et al.*,<sup>50</sup> the temperature of the hot plate is 400 °C, where the corresponding Jacob number  $Ja = 0.51$ . The droplet diameter is 2.3 mm and the impacting velocity is 0.63 m/s, leading to Weber number  $We = 15.7$ . The comparison of results is shown in Fig. 4(a), and qualitative agreement between the simulation and experimental results is achieved. Similar to Ref. 26, we quantitatively compare the evolution of droplet gravity central height ( $\epsilon_{mass}$ ) with the experimental data. In our simulation, the height of the droplet gravity center is calculated by

$$\epsilon_{mass} = \frac{\sum_{\rho > \rho_{avg}} \rho(\mathbf{x})h(\mathbf{x})}{\sum_{\rho > \rho_{avg}} \rho(\mathbf{x})}, \quad (15)$$

where  $h(\mathbf{x})$  is the height of each cell and  $\rho(\mathbf{x})$  represents the density of the cell. As indicated in Fig. 4(b), after the droplet touches the plate, owing to the deformation of the droplet,  $\epsilon_{mass}$  decreases from the center of the sphere ( $R_0$ ). After  $\epsilon_{mass}$  reaches the minimum value during the spreading stage, it increases due to the droplet recoiling and rebound. The simulation results are in line with previous experimental data.<sup>50</sup> Additionally, we conduct a mesh independency study by increasing the mesh resolution to  $dx = R_0/60$  or decreasing to  $dx = R_0/45$ . As shown in Fig. 4(b), the evolution processes of  $\epsilon_{mass}$  for all cases are consistent, which support the conclusion that the current mesh resolution ( $dx = R_0/50$ ) is sufficiently fine for simulation.

The last validation is based on the experiment conducted by Bianco *et al.*,<sup>51</sup> corresponding to the experimental configurations and the simulation setup of case 3 in Table I. The comparison in Fig. 5(a) is for a water droplet ( $R_0 = 1$  mm) impacting a 300 °C flat plate with an initial velocity at 0.8 m/s. As presented in the figure, our simulation results are generally consistent with the experiment results. Some

deviations between the simulation and experimental snapshots can be found before the droplet bouncing, possibly because temperature-independent thermal properties are used in the current simulation. Besides, the constant contact temperature in our simulation may overestimate the evaporation rate of the droplet. Compared with the realistic situation, this setting could lead to a thicker vapor film between the droplet and the heated plate. Nevertheless, the current LBM model still provides a reliable prediction for the Leidenfrost droplet impingement, notably the thin vapor film between the droplet and hot plate, as well as the droplet bouncing owing to the Leidenfrost effect.

We then extend the simulation in Fig. 5(a) to a wider range of impact Weber numbers by increasing the droplet initial velocity, with all the other setups kept the same. We qualitatively compare the normalized droplet contact time ( $t_c^*$ ) and maximum spreading factor ( $\beta_{max}$ ) with the experimental data<sup>51</sup> and theoretical predictions. Figure 5(b) indicates the droplet contact time under various Weber numbers. In the figure, the droplet contact time is normalized by  $t_c^* = Ut_c/D_0$ . In previous literature,<sup>26,52,53</sup> the theoretical contact time of the Leidenfrost droplet is approximately predicted by Rayleigh's theory,<sup>8</sup>  $t_c/\tau = \pi/4$ , where  $\tau = (D_0^3 \rho_l/\sigma)^{0.5}$  is the inertia-capillarity time. Thus, the normalized droplet contact time can be re-written as

$$t_c^* = \frac{t_c U}{D_0} = \frac{\pi U}{4 D_0} \sqrt{\frac{D_0^3 \rho_l}{\sigma}} = \frac{\pi}{4} \sqrt{We}. \quad (16)$$

We plot Eq. (16) as a solid line in Fig. 5(b). As shown in the figure, our simulation results are in excellent agreement with the experimental data<sup>51</sup> and theoretical results, for a wide range of Weber numbers. Another comparison is conducted for the droplet maximum spreading diameter. In this case, the maximum spreading factor of the droplet is defined as  $\beta_{max} = D_{max}/D_0$ , where  $D_{max}$  is the droplet maximum spreading diameter. The simulation results are compared with experiments (Bianco *et al.*,<sup>51</sup> represented by solid square symbols, and Riboux and Gordillo,<sup>54</sup> by solid circle symbols) as well as the power law fitting equation (solid line)  $\beta_{max} = \alpha We^{0.25}$ , where the pre-factor  $\alpha = 0.85$  is achieved by the experimental fitting.<sup>51</sup> We also compare

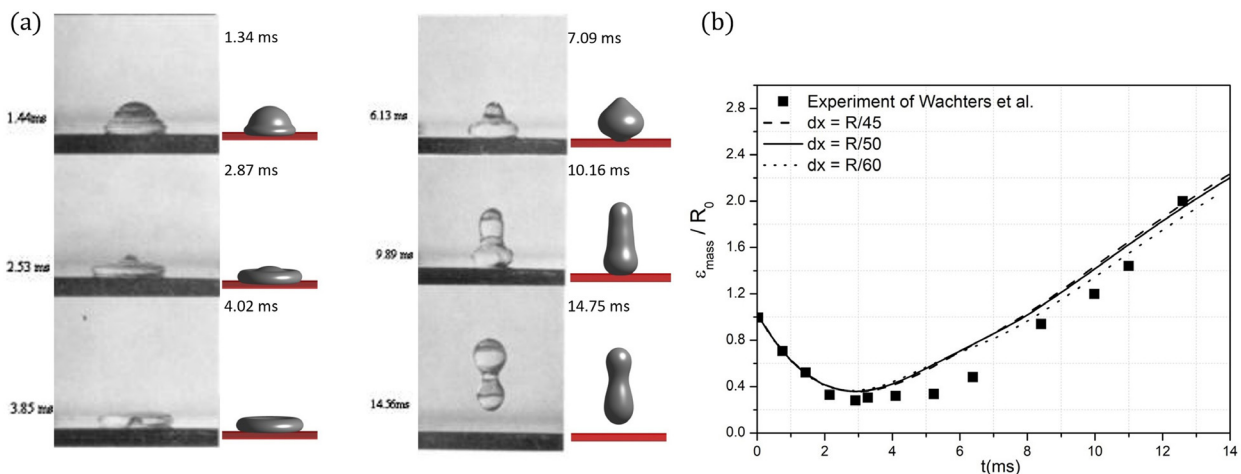
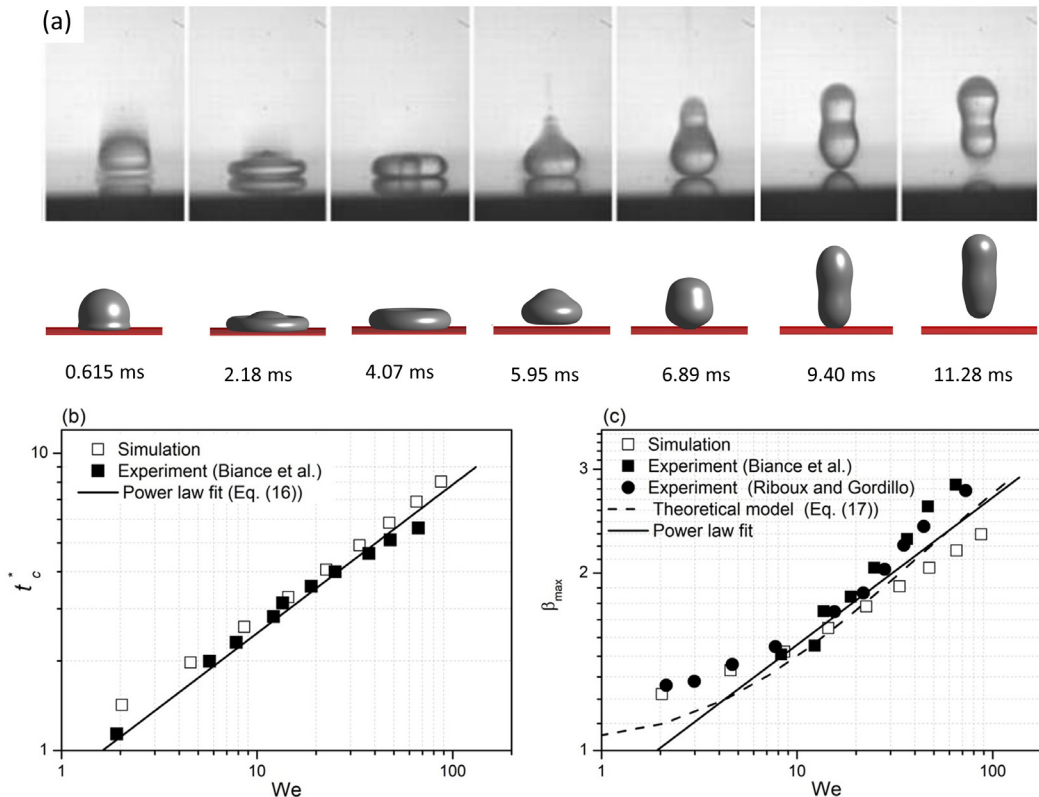


FIG. 4. (a) A qualitative comparison of simulation results (right column) and experiment snapshots (left column) of droplet impact on a heated plate with  $We = 16$ ,  $Ja = 0.61$ . (b) Transient evolution of the height of the dimensionless droplet gravity center ( $\epsilon_{mass}/R_0$ ), the lines represent the simulation results with various mesh resolutions and the symbols indicate the experiment results in Ref. 26.



**FIG. 5.** (a) Comparison of the experimental snapshots (top column) and simulation results (bottom column) of droplet impact on a heated plate at  $We = 21.5$ ,  $Ja = 0.5$ . (b) The normalized droplet contact time ( $t_c^*$ ) as a function of Weber number, the simulation results (solid square symbols) are compared with the power law fitting equation [Eq. (16), solid line in the figure] and experiment results (hollow square symbols). (c) Comparison of the simulated droplet maximum spreading factors ( $\beta_{max}$ , hollow square symbols) with experiment results (solid symbols), experimental power law fitting equation (solid line) and theoretical prediction equation (dashed line).

our results with the energy balance based theoretical equation (dashed line in the figure) for  $\beta_{max}$ , where<sup>55</sup>

$$(\beta_{max}^2 - 1)^{0.5} \left( \frac{\sqrt{We}}{Oh} \right)^{-0.2} = \frac{\sqrt{We}}{\sqrt{We} + 7.6}. \quad (17)$$

As presented in Fig. 5(c), our simulation results are in line with the power-law fitting and theoretical equations, for a wide range of Weber numbers. It can be found that  $\beta_{max}$  in our simulations is somewhat lower than the experimental results at larger Weber numbers. This is because, in our simulations, a fixed viscosity is used and the viscous effects are overestimated for high Weber number cases, which results in a lower  $\beta_{max}$ .

### III. RESULTS AND DISCUSSION

#### A. Simulation setup

Having validated our multiphase thermal LB model within the ULBM framework against experimental and theoretical results, we then simulate a droplet with  $D_0 = 1.7$  mm impacting an overheated plate with square pores, with a corresponding Bond number  $Bo = 0.12$ . The simulation configuration is shown in Fig. 6(a). In the following, the simulation domain is set as a  $700 \times 700 \times 720$  box. The other setups (e.g., initial droplet radius, thermal properties of the fluid

and boundary conditions) kept exactly the same as the validation cases in Sec. II C. The detailed structure of the plate with square pores is shown in Fig. 6(b). The depth of the pores ( $H_p$ ) is kept as 40 in lattice unit (0.8 mm), the diameter of the equal size pores is  $D_p$ , and the intervals between the pores are  $L$ . In the following simulations, the Jacob number is kept higher than 0.5 to ensure the plate temperature is over the Leidenfrost point. It also needs to be mentioned that the minimum thickness of the vapor layer between the liquid and solid plate (the minimum distance of the liquid above the plate to the plate's upper surface,  $\epsilon_{min}$  in the figure) is recorded. The droplet spreading factor during the evolution is defined as  $\beta = D/D_0$ .

#### B. The influence of the Weber number

First, we aim to investigate the influence of the impact Weber number at various plate temperatures and configurations. In this section,  $D_p$  and  $L$  are fixed as 11 lattices (220  $\mu\text{m}$ ) and 4 lattices (80  $\mu\text{m}$ ), respectively. Two different plate temperatures are considered: one with Jacob number  $Ja = 0.52$  for  $T_h \approx 400^\circ\text{C}$  and the other with Jacob number  $Ja = 0.7$  for  $T_h \approx 500^\circ\text{C}$ . The other simulation setups kept the same as in Sec. II C. We change the impact Weber numbers from 4.6 to 87.4 by changing the droplet initial velocities. Evolutions of the droplet shape are shown in Fig. 7. For ease of comparison and



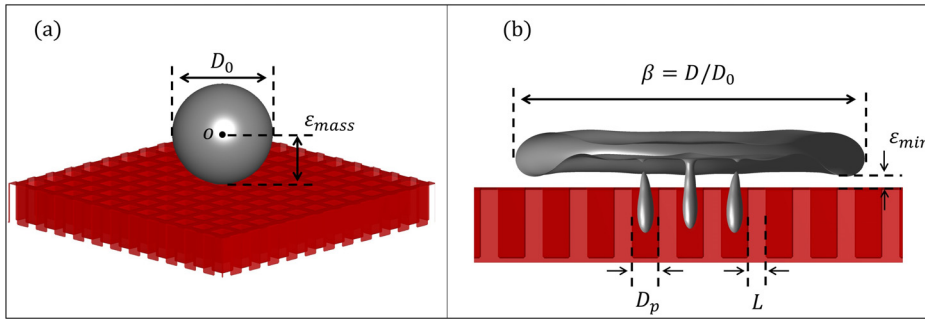


FIG. 6. Illustrations of the simulation configuration: (a) 3D main view of droplet initial state. (b) Half cutaway view during the droplet evolution.

observation, the droplet is shown as a half cutaway view, and a main view snapshot of the droplet is shown in the last frame.

Figure 7(a) demonstrates the evolution of the Leidenfrost droplet impact on a flat plate. It is noticed that an air pocket is formed during the droplet spreading ( $t/\tau = 0.35$ ), which has also been observed in previous simulations and experiments.<sup>56,57</sup> The trapped air in the pocket is caused by the droplet evaporation during the spreading, and the pocket-like geometry of the vapor is attributed to the effect of buoyancy force.<sup>29</sup> The pocket neck breaks ( $t/\tau = 0.35$ , marked by black dashed circles) owing to different flow scales within the droplet and the trapped air in air pocket.<sup>56</sup> This consequently levitates the droplet from the plate and exhausts the entrapped air. Nevertheless, the levitated droplet re-contacts the plate during the recoiling period

and then completely bounces off from the plate when  $t/\tau = 0.87$ . Figure 7(b) shows the droplet impact on an overheated porous plate at the same Weber number and Jacob number. As shown in the figure, the droplet demonstrates similar morphologies during its evolution. However, it can be observed that a part of the droplet penetrates into the pores ( $t/\tau = 0.04$ ) and then evaporates ( $t/\tau = 0.2$ ). The generated vapor layer ( $t/\tau = 0.36$ ) is thicker and the droplet rebounds faster ( $t/\tau = 0.78$ ) in this case than the case with a flat plate.

The droplet demonstrates different morphologies when impacting the overheated porous plate at a larger Weber number. As shown in Fig. 7(c), owing to a higher Weber number, more liquid penetrates into the pores at the beginning of impingement ( $t/\tau = 0.042$ ) and evaporates. Remarkably, the droplet directly rebounds from the plate

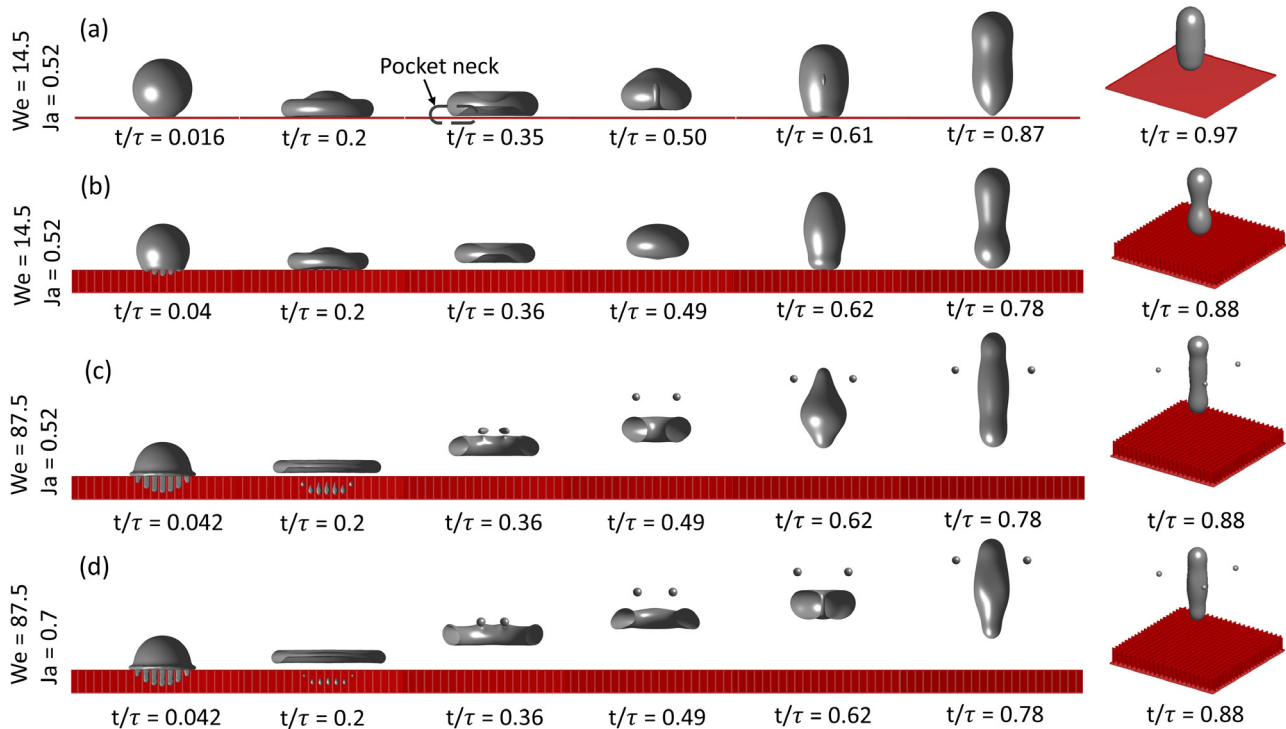
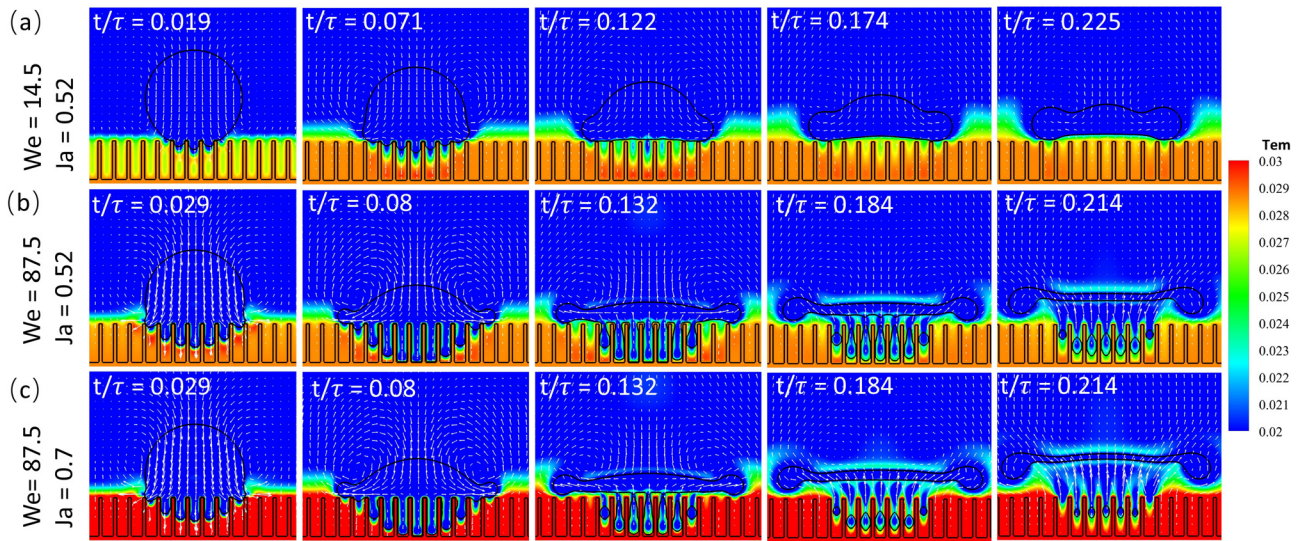


FIG. 7. Snapshots for a droplet impact on a heated plate with various  $We$  and  $Ja$ . (a) is for a droplet impacting a flat plate and (b)–(d) are for a droplet impacting a porous plate.



**FIG. 8.** Illustrations of temperature distributions, velocity vectors, and morphology evolutions of the droplet at the early stage of impacting a heated porous plate. (a)–(c) stands for various  $We$  and  $Ja$  cases.

before its recoiling ( $t/\tau = 0.2$ ) in a pancake shape. Additionally, a similar pancake-like bouncing phenomenon has also been observed in the previous experiments for the droplet impact on high-temperature nanotube surfaces,<sup>21,23</sup> heated surfaces in the depressurized environment,<sup>58</sup> superheated micropillars surfaces,<sup>59,60</sup> as well as superheated micropores surfaces.<sup>20</sup> In addition, this pancake bouncing phenomenon can also be observed when a droplet impacts a higher temperature porous plate, as shown in Fig. 7(d).

Then, we give a detailed analysis of the mechanism of this unique bouncing phenomenon. The transient evolutions of droplet profiles (black lines), velocity vectors (white vectors, with a fixed scale to the velocity magnitude), and temperature distributions during the spreading stage are shown in Fig. 8. Comparing cases with the same plate temperature but different Weber numbers [Figs. 8(a) and 8(b)], we find that more liquid penetrates into the heated pores during the droplet spreading stage for the larger Weber number case [ $t/\tau = 0.08$  in Fig. 8(b)]. With the continuous evaporation of the penetrated liquid in pores, entrapped air is formed between the droplet bottom part and the heated plate. Thus, the larger the amount of evaporated liquid, the

more entrapped air will be generated. In other words, the entrapped air generated by the evaporated liquid will provide a larger pressure force [comparing Figs. 9(b) and 9(c) with Fig. 9(a)], because most of the impacting kinetic energy of the droplet has been transformed into surface energy during the spreading stage. Therefore, when the pressure force is larger than the gravity and vertical dynamic force, the droplet bounces from the plate [ $t/\tau = 0.214$  in Fig. 8(b)]. The same dynamics can also be found in the case with a higher Jacob number (plate temperature). As shown in Fig. 8(c), similarly, we can observe the penetration and evaporation of the liquid inside the pores. In the case with a higher plate temperature, the liquid evaporation is faster. Thus, we can find the liquid disk rebounds with a higher velocity [seeing the velocity vectors in Fig. 8(c) when  $t/\tau = 0.214$ ].

Notably, satellite droplets can be observed during the droplet bounce in Figs. 7(c) and 7(d). The generation of the satellite droplets is owing to the breakup of thin liquid lamella during droplet spreading. A 3D main view for the selected cases is shown in Fig. 10 to demonstrate the evolution of the liquid lamella. Comparing cases with a flat plate and a porous plate for the same Weber number [Figs. 10(a) and 10(c)],

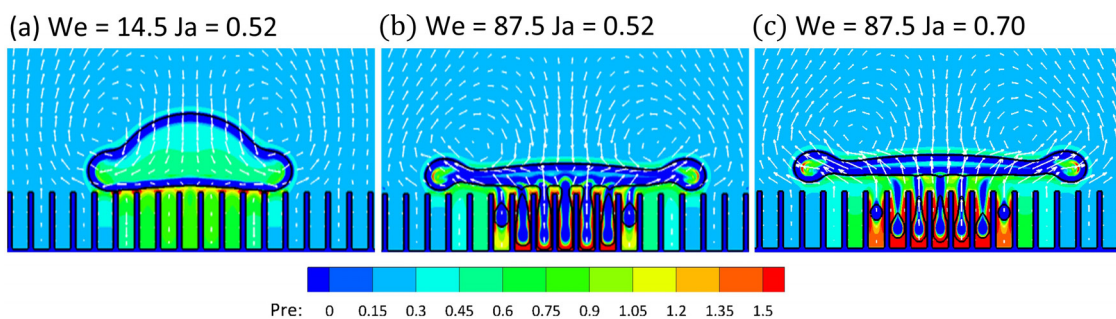


**FIG. 9.** Illustrations of pressure distributions, velocity vectors, and morphologies of a Leidenfrost droplet impacting heated porous plate at  $t/\tau = 0.13$ . (a)–(c) stand for various  $We$  and  $Ja$  cases. The pressure in the figure is normalized by  $P_c$ .

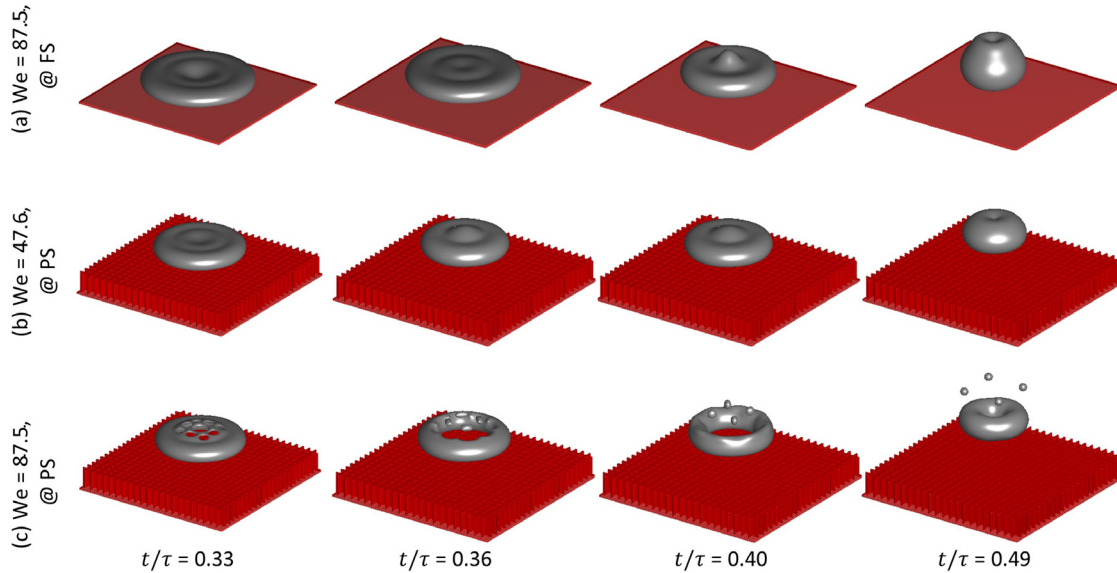


**FIG. 10.** Illustrations of the liquid lamella evolution at  $Ja = 0.52$ . (a) Droplet impacts a flat plate, at  $We = 87.5$ . (b) Droplet impacts a porous plate, at  $We = 47.6$ . (c) Droplet impacts a porous plate, at  $We = 87.5$ .

liquid flows into pore spaces, making holes in the lamella after impingement on the porous plate. Then, with the spreading of the liquid lamella, the liquid bridges between the holes breakup from edges [seeing  $t/\tau = 0.36$  in Fig. 10(c)], and the fragmented liquid bridges retract and form satellite droplets [seeing  $t/\tau = 0.4$  in Fig. 10(c)]. However, comparing cases with a porous plate but different impact Weber numbers [Figs. 10(b) and 10(c)], the liquid lamella remains intact for the lower Weber number case, which is due to the fewer penetrated liquid and the thicker spreading lamella.

The evolution of  $\epsilon_{min}/D_0$  for selected cases is recorded and plotted in Fig. 11(a). As indicated in the figure, for all cases, a peak value of  $\epsilon_{min}$  can be found before droplet recoiling. This phenomenon has also been recorded in recent simulation studies for the droplet impact

on an overheated flat plate.<sup>9,35,61</sup> The peak value of  $\epsilon_{min}$  corresponds to the instant when the droplet kinetic energy is minimized, and therefore, the trapped air is exhausted. Then, the droplet re-contacts the plate during the recoiling with some small oscillations. Finally, the droplet bounces from the plate. The period from the droplet's first touch on the plate to its bounce off the plate is defined as the contact time ( $t_c$ ). As shown in Fig. 11(a), the peak value of  $\epsilon_{min}$  increases slightly with the Weber number for the droplet impact on a flat surface (FS). Nevertheless,  $\epsilon_{min}$  increases significantly with the Weber number for droplet impact on a porous surface (PS). This implies the additional lift force provided by the entrapped air is similar in cases for droplet impact on a flat surface. On the contrary, the additional lift force increases significantly with the Weber number in cases of the

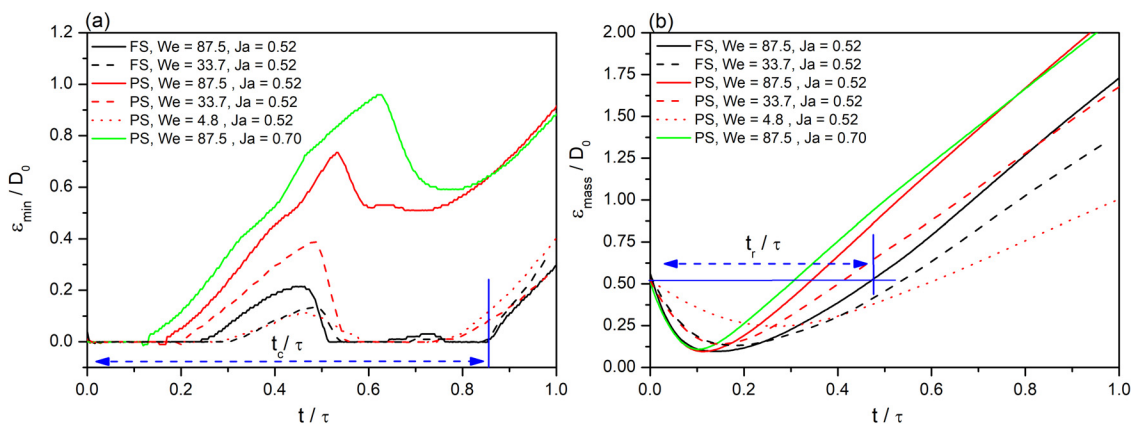


**FIG. 11.** (a) Transient evolution of the normalized vapor layer thickness  $\epsilon_{min}/D_0$ , and different lines stand for the cases with various  $We$ ,  $Ja$  and plate configurations. The period shown in the figure represents the droplet contact time ( $t_c$ ). (b) Evolution of the normalized droplet gravity center  $\epsilon_{mass}/D_0$  for different cases, and the period shown in the figure represents the droplet rebound time ( $t_r$ ).

droplet impact on a porous surface. This is attributed to the evaporated liquid inside the pores. Consistent with the qualitative results, it can be found that the droplet directly bounces off from the plate during the spreading stage for the larger Weber number cases in the porous plate.

We also record the evolution of  $\epsilon_{mass}$  and plot the evolution of  $\epsilon_{mass}/D_0$  in Fig. 11(b), whose value can be used to quantify the speed of droplet retraction and bouncing. As shown in the figure, after the droplet touches the plate,  $\epsilon_{mass}$  decreases from the center of the sphere ( $\epsilon_{mass}/D_0 = 0.5$ ) to a minimum value. In addition, it can be found that the decay rate and the minimum value of  $\epsilon_{mass}$  are almost the same in cases with the same Weber number, regardless of different Jacob numbers and plate geometries (FS or PS). The same tendency of  $\epsilon_{mass}$  for the same Weber number cases during the decay stage can be explained by the spreading and collapse of the droplet disk governed by the inertial effect.<sup>62</sup> Thus, the penetrated liquid inside the pores has little influence on the droplet spreading dynamics [comparing Figs. 7(a) and 7(b), at  $t/\tau < 0.36$ ]. However, the rebound velocities are different for different cases. Under the same operating conditions, it is found that the droplet rebound velocity increases with the Weber number, and the rebound velocity is always higher in the cases of

droplet impact on a porous plate. This result can further reveal the fact that the pressure force generated by the evaporated liquid inside the pores contributes to the droplet bounce. As shown in the figure, we define the period between the droplet's first contact with the plate to  $\epsilon_{mass}/D_0 > 0.5$  (the initial position of  $\epsilon_{mass}$ ) as the droplet rebound time ( $t_r$ ).

The dimensionless droplet contact time ( $t_c/\tau$ ) and droplet diameters when the droplet leaves the plate [ $D(\uparrow)/D_{max}$ ] for all cases are recorded in Figs. 12(a) and 12(b), respectively. Consistent with the results in Sec. II C, for cases of the droplet impact on a heated flat plate, dimensionless droplet contact time ( $t_c/\tau$ ) almost remains constant for a wide range of Weber number as shown in Fig. 12(a). For the droplet impact on a porous plate at the same Jacob number [hollow triangle cases in Fig. 12(a)], it always presents a shorter  $t_c$  compared with the droplet impact on a flat plate. Notably, a significant decrease in  $t_c$  is observed as the Weber number increases, which corresponds to the pancake bouncing cases. It is also found that, with the increase in the Jacob number, both  $t_c$  and the minimum Weber number for the pancake bouncing phenomenon keep decreasing. At lower Weber numbers, the lifting diameter  $D(\uparrow)$  is similar for all the cases despite various plate geometry and plate temperature, while the pancake bouncing doubles the lifting diameter at higher Weber numbers.

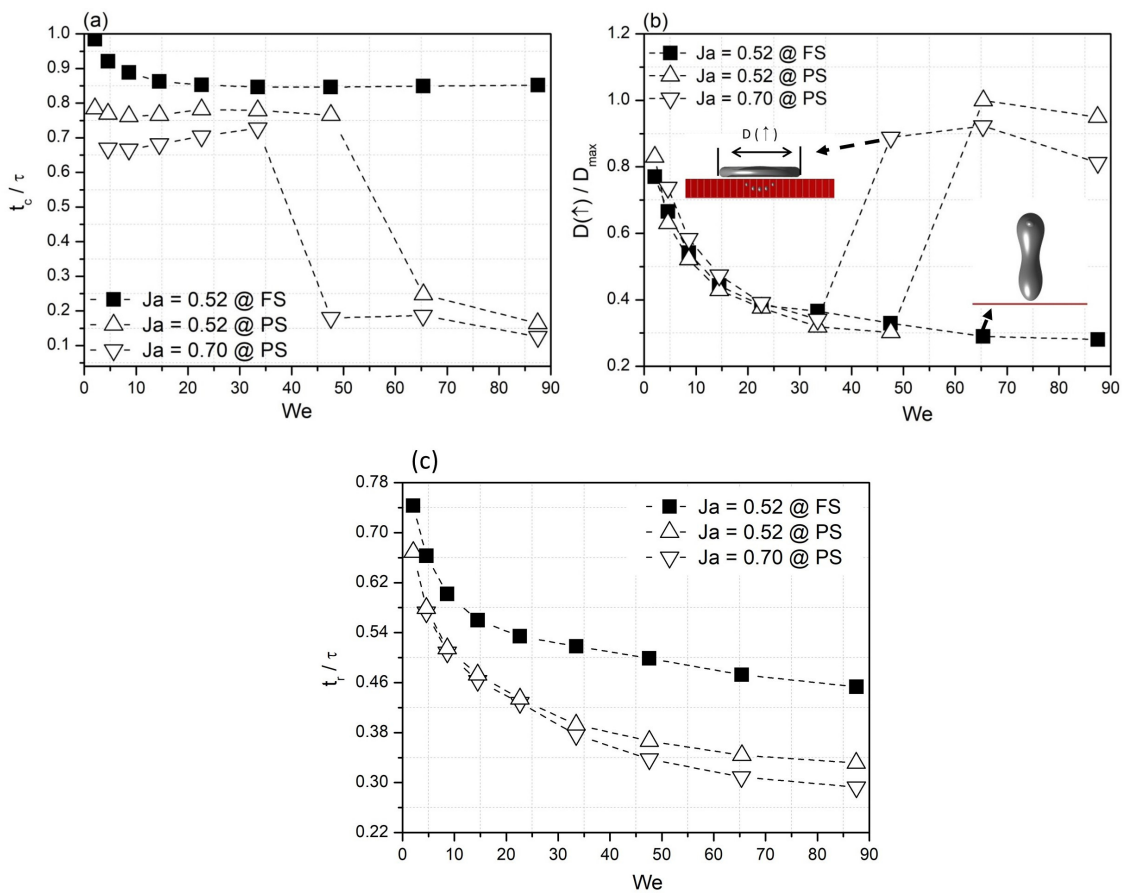


FIG. 12. Normalized (a) droplet contact time  $t_c/\tau$ , (b) the droplet diameters when it leaves the plate  $D(\uparrow)/D_{max}$ , and (c) droplet rebound time  $t_r/\tau$  as a function of impacting  $We$  for the cases with various  $Ja$  and plate morphologies.

It should be pointed out that the observed pancake bouncing for droplet impact on a heated porous plate has a different mechanism from the previous pancake bouncing due to the droplet impact on superhydrophobic surfaces.<sup>63–65</sup> For the droplet pancake bouncing on textured superhydrophobic surfaces, the lift force is provided by the capillary force. For droplet impacting a heated porous plate, as discussed above, the lift force is generated by the pressure force of the evaporated liquid (indicated in Fig. 9). In addition, it is found that the penetrated liquid remains in the pores when the droplet bounces from the plate at  $t/\tau = 0.2$  [seeing Figs. 7(c) and 7(d)], which contrasts sharply with the retracting droplet pancake bouncing when droplets impact textured surfaces.<sup>64,66</sup>

The evolution of normalized droplet rebound time ( $t_r/\tau$ ) for all cases is recorded and plotted in Fig. 12(c). As shown in the figure, for all cases,  $t_r$  decreases with Weber number. This is because, for the larger Weber number case, the surface tension is smaller compared with the dynamic force; thus, the droplet recoils earlier, which can be proved in Fig. 11(b) (for the larger  $We$  cases,  $\epsilon_{mass}$  reaches the minimum value earlier). Additionally, in agreement with the results in Figs. 7 and 12(a), impact cases on a porous plate always produce shorter  $t_r$  compared with flat plate impact cases.  $t_r$  is further decreased for the higher Jacob number cases at the large Weber number. The results in Fig. 12(c) confirm the previous analysis, where the additional lift force provided by the evaporated liquid accelerates the droplet rebound.

The modified droplet maximum spreading time  $t_{max}/\tau'$  [the period when the droplet reaches the maximum spreading diameter,  $\tau' = (D_{max}^3 \rho_l / \sigma)^{0.5}$ ] as a function of the Weber number is plotted in Fig. 13(a). It indicates that  $t_{max}/\tau'$  is almost identical for different cases at the same Weber number, and  $t_{max}/\tau'$  indicates a power-law decay dependency with the increase in the Weber number. In the study of Lin et al.,<sup>67</sup> they proposed the following equation to predict  $t_{max}$ :

$$\frac{t_{max}}{(D_{max}^3 \rho_l / \sigma)^{0.5}} = \zeta We^{-0.43}, \quad (18)$$

where  $\zeta$  is the experiment fitting constant. It should be noticed that the term  $(D_{max}^3 \rho_l / \sigma)^{0.5}$  on the right-hand side of Eq. (18) can be regarded as the modified inertia-capillarity time ( $\tau'$ ) referring to a droplet of size  $D_{max}$ . The experimentally fitted universal value for  $\zeta$  is 0.44 in Ref. 67 and the corresponding equation is plotted in Fig. 13(a) for comparison. By fitting our simulation results in Fig. 13(a), we can see, our simulation results also follow the  $\sim We^{-0.43}$  power law dependency. Note that, our fitted prefactor  $\zeta = 0.55$  is slightly higher than

the experimental value, which however matches the high viscosity cases in Ref. 67.

Figure 13(b) demonstrates  $\beta_{max}$  as a function of Weber number for all cases. Consistent with the results in Fig. 13(a), it can be found that both Jacob number and plate geometries almost have no influence on  $\beta_{max}$ . For all cases,  $\beta_{max}$  increases with Weber number with a power law dependency. The best fitted equation for  $\beta_{max}$  in our study is

$$\beta_{max} = 1.05 We^{0.17}, \quad (19)$$

where the perfect 1.05 is in good agreement with the fitted experimental results in Ref. 51 but the index 0.17 is slightly lower than 0.25 in the experiment. We also plot the theoretical prediction Eq. (17) as the dashed line in the figure, and it can be observed all simulation results are in line with the theoretical equation. Notably, for the same reason as pointed out in Sec. II C, the simulated  $\beta_{max}$  is lower than the theoretical value at the larger Weber numbers. In addition, this leads to a lower index in our best fitted exponential equation than that in Ref. 51.

Finally, the dimensionless droplet evaporation mass ( $M_e/M_0$ ) and the averaged heat flux ( $Q_{avg.}$ ) during the period  $t = 0 \sim t_r$  are plotted in Figs. 14(a) and 14(b), respectively. The heat flux of each time instant is calculated as

$$q = \frac{1}{L_x L_y} \iint \left[ -\lambda \left( \frac{\partial T}{\partial z} \right) \Big|_{(z=H_p)} \right] dx dy, \quad (20)$$

where  $L_x$  and  $L_y$  are the length of the simulation domain in x and y directions, respectively. As shown in Fig. 14(a),  $M_e/M_0$  almost increases linearly with Weber numbers, and the evaporation mass is almost the same for two different Jacob number cases. A cylinder model is used to explain the linear relationship between  $M_e/M_0$  and Weber number. We assume that the maximum deformation of the droplet in the horizontal direction still follows  $r_{max} \sim We^{0.25}$  dependency as reported in Refs. 51 and 68. In addition, as mentioned above, the collapse of the droplet disk is governed by the inertial effect, and the dynamic force is minimized when  $t = t_{max}$ . Thus, the maximum penetration length of the liquid slug inside the pores has the relationship of  $h_{max} \sim Ut_{max} \sim We^{0.445}$ , where  $t_{max}$  is described as Eq. (18). Considering the penetrated liquid ( $M_p$ ) can be regarded as a cylinder shape and be completely evaporated owing to the high plate temperature and small pores size ( $D_p/D_0 < 0.1$ ), the evaporation mass can be

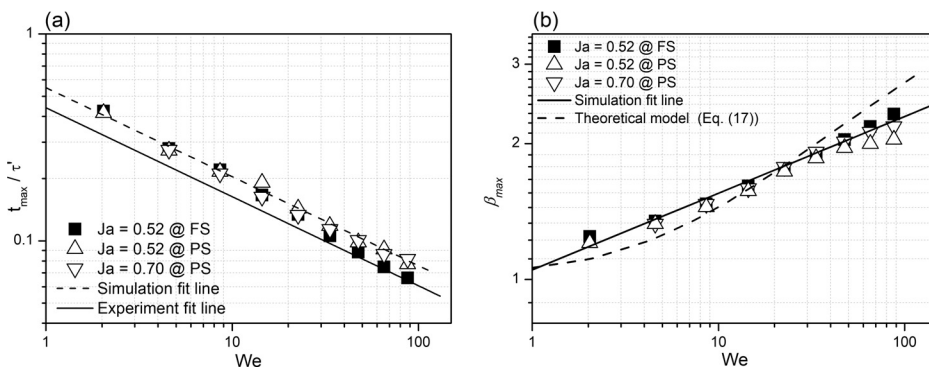
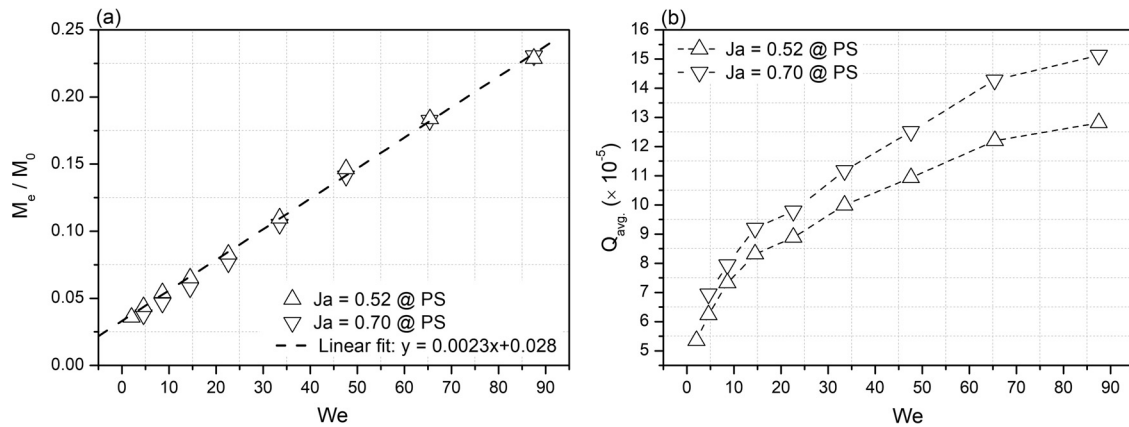


FIG. 13. (a) The modified droplet maximum spreading time  $t_{max}/\tau'$ , where  $\tau' = (D_{max}^3 \rho_l / \sigma)^{0.5}$ , (b) droplet maximum spreading factor  $\beta_{max}$  as a function of impacting  $We$ , the different symbols in the figure indicates various  $Ja$  and plate configurations. The lines in the figure stand for the theoretical prediction equations and fitted power law function.



**FIG. 14.** The relation of (a) the dimensionless droplet evaporation mass  $M_e/M_0$  and (b) time averaged heat flux  $Q_{avg}$ , with a variety of impacting  $We$ . The results are for droplet impact on a heated porous plate with different  $Ja$ , from  $t = 0 \sim t_r$ . The dashed line in (a) represents a linear fitting function.

scaled as  $M_e/M_0 = M_p/M_0 \sim h_{max}r_{max}^2 \sim We^{0.945} \approx We$ . For the time averaged heat flux shown in Fig. 14(b),  $Q_{avg}$ , generally increases with the Weber number, which can be explained by the fact that a higher  $We$  leads to a higher liquid contact area (larger  $\beta_{max}$ ) and a higher spreading velocity (shorter  $t_{max}$ ). Consequently, this enhances the phase change heat transfer and convective heat transfer. Considering  $\beta_{max}$  and  $t_{max}$  are almost the same for various Jacob numbers at the same Weber number, it can be understood that the higher plate temperature cases demonstrate higher heat flux.

**C. The influence of pore intervals**

In this section, we investigate the influence of the pore intervals. In the following simulations,  $D_p$  is fixed as nine lattices ( $180 \mu m$ ), and  $L$  is changed from 1 lattice ( $20 \mu m$ ) to 97 lattices ( $1.9 mm$ ), which leads to the dimensionless pore intervals  $L^* = L/D_0$  varying from 0.01 to 0.99. For all the cases in this section, Weber number  $We = 69.2$  and Jacob number  $Ja = 0.7$ , and all the other setups are the same as in Sec. III B.

Figure 15 shows qualitative evolutions of the droplet shape as it impacts porous plates with various  $L^*$ . Similar to the results in Fig. 7, after the droplet impacts the porous surface, a part of the droplet penetrates into the pores and evaporates. After that, the droplet levitates from the plate during the spreading and the entrapped air is exhausted. As indicated in the figure, for the smaller  $L^*$  case [Fig. 15(a)], owing to the smaller solid fraction, more liquid penetrates into the pores and evaporates. As pointed out in the above analysis, the more evaporated liquid, the larger pressure force will be provided. Consequently, the droplet presents the pancake bouncing for the smaller  $L^*$  cases [similar to the phenomena in Figs. 7(c) and 7(d)]. For the larger  $L^*$  cases [Figs. 15(b) and 15(c)], it can be observed that the droplet re-touches the plate during the recoiling stage and then bounces from the plate, which is similar to the morphologies in Fig. 7(b).

The early stage evolutions for two different  $L^*$  cases are shown in Fig. 16. Consistent with the previous findings, regarding the lower  $L^*$  case, more liquid penetrates into the pores [ $t/\tau = 0.077$  in Fig. 16(a)]

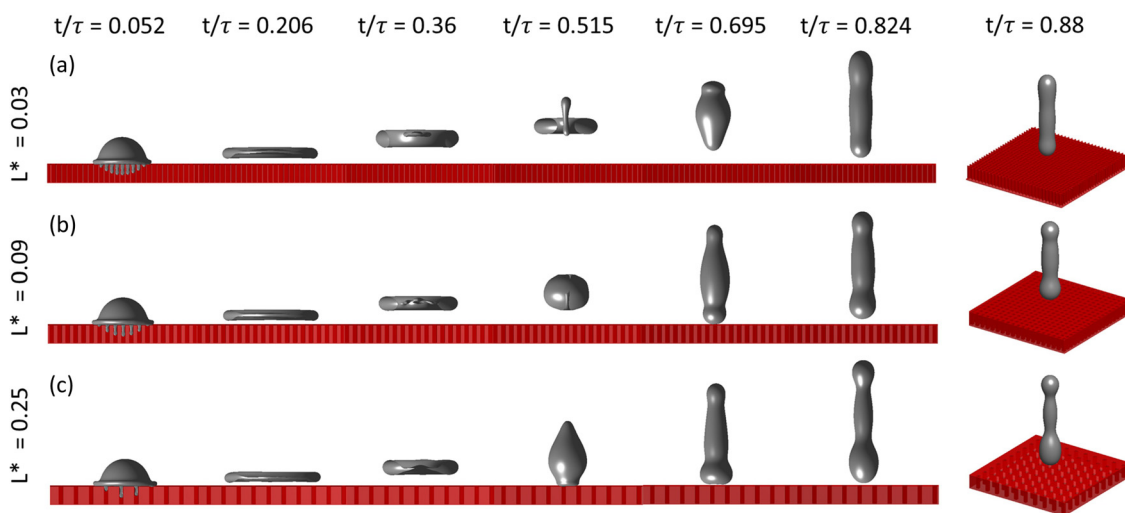


**FIG. 15.** Qualitative evolutions of droplet impact on a porous plate with various pore intervals  $L^*$ ,  $We = 69.2$ , and  $Ja = 0.7$ . (a)  $L^* = 0.03$ , (b)  $L^* = 0.09$ , and (c)  $L^* = 0.25$ .

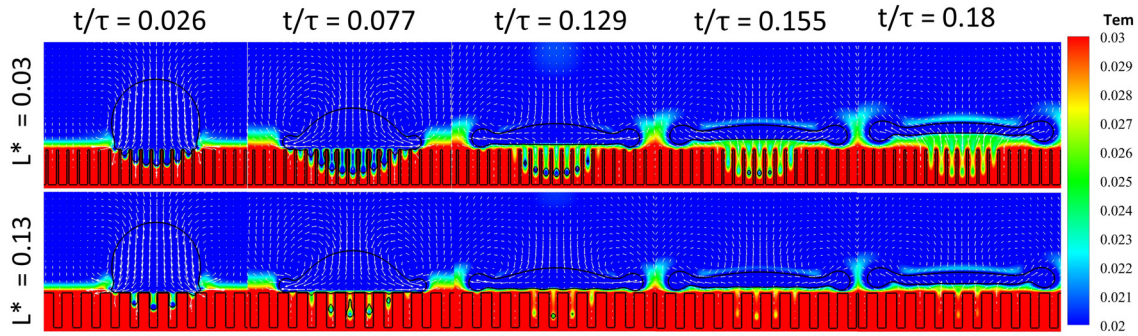


FIG. 16. The temperature contours, velocity vectors and morphology evolutions of the droplet at the early stage of impact on a heated porous plate with different pore intervals.

and then evaporates [ $t/\tau = 0.129$  in Fig. 16(a)]. Qualitatively, it can be found that the droplet morphologies for various  $L^*$  cases are similar in the early spreading stage. Nevertheless, the larger quantity of evaporated liquid provides a larger pressure force and finally leads to the droplet bouncing from the plate [ $t/\tau = 0.18$  in Fig. 16(a)]. It can also be confirmed by the temperature field inside the pores that for the lower  $L^*$  case, the temperature is lower due to the more significant evaporation cooling effect by its larger evaporation rate.

The transient evolution of droplet spreading ratio for various  $L^*$  cases is plotted in Fig. 17(a). As shown in the figure, the droplet first spreads to the maximum value and then recoils. Concurring with the qualitative results in Fig. 16, the spreading ratio is identical for a wide range of  $L^*$ .  $\beta_{max}$  (left axis, represented by solid squares) and  $t_{max}/\tau'$  (right axis, represented by solid circles) in relation to  $L^*$  is plotted in Fig. 17(b). As shown in the figure, consistent with the qualitative observation in Fig. 15, both  $\beta_{max}$  and  $t_{max}/\tau'$  are almost at a constant value for a wide range  $L^*$ , which can be observed in Fig. 17(a). The identical  $\beta_{max}$  and  $t_{max}$  can be explained by the fact that the droplet spreading stage is dominated by the inertia effect. In other words, the penetrated liquid inside pores has little influence on the droplet dynamics in the horizontal direction. Consequently,  $\beta_{max}$  and  $t_{max}$  present similar values in the same Weber number, regardless of different values of  $L^*$ . Additionally, the predicted value of  $t_{max}$  by Eq. (18)

and  $\beta_{max}$  by Eq. (19) are plotted in Fig. 17(b) by dashed and solid lines, respectively. It can be observed that the theoretical equations can also give good predictions of  $\beta_{max}$  and  $t_{max}$  for a wide range of  $L^*$ .

The evolution of  $\epsilon_{mass}/D_0$  is plotted in Fig. 18(a), and  $t_r/\tau$  as a function of  $L^*$  is shown in Fig. 18(b). It can be observed that the evolution of  $\epsilon_{mass}$  during the decay stage for all cases is almost constant. During the rebound stage, the minimum  $L^*$  presents the fastest rebound speed and shortest rebound time ( $t_r$ ). For the larger  $L^*$  cases during the rebound stage, the evolutions of  $\epsilon_{mass}$  are very similar (e.g.,  $L^* = 0.25$  and  $L^* = 0.97$ ). It should be mentioned that the solid fraction of the porous plate can be calculated as  $\phi = 1 - (D_p/(D_p + L))^2$ ,  $D_p$  is fixed as 9 lattices when changing  $L$ . As a result, the corresponding  $\phi$  varies from 0.9 to 0.99 when  $L^*$  is changed from 0.2 to 0.97, which implies that only a small amount of liquid penetrates into the pores when  $L^* > 0.2$ , and the amount of the evaporated liquid is very small. Consequently, the pore intervals have slight influence on droplet dynamics. For a similar reason, we can find  $t_r$  remains at a similar value when  $L^* > 0.2$  [as shown in Fig. 18(b)]. This can also explain why  $\beta$  [Fig. 17(a)] and  $\epsilon_{mass}$  [Fig. 18(a)] present similar evolution trends for the high  $L^*$  cases.

We record  $M_e/M_0$  ( $t = 0 \sim t_r$ ) as a function of the plate opening fraction  $1 - \phi$  in Fig. 19. As shown,  $M_e/M_0$  is linearly increased with  $1 - \phi$ . Additionally, we can find  $M_e$  is significantly increased

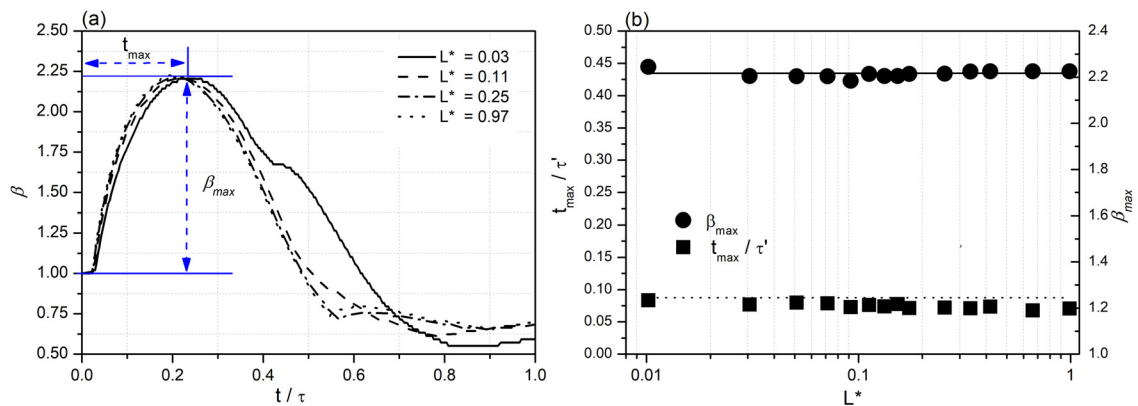


FIG. 17. (a) Transient evolution of droplet spreading ratio  $\beta$  for various  $L^*$  cases. (b)  $t_{max}/\tau'$  (right axis) and  $\beta_{max}$  (left axis) as a function of  $L^*$ , the dashed line and solid line stand for the predicted value calculated by Eqs. (18) and (19), respectively.

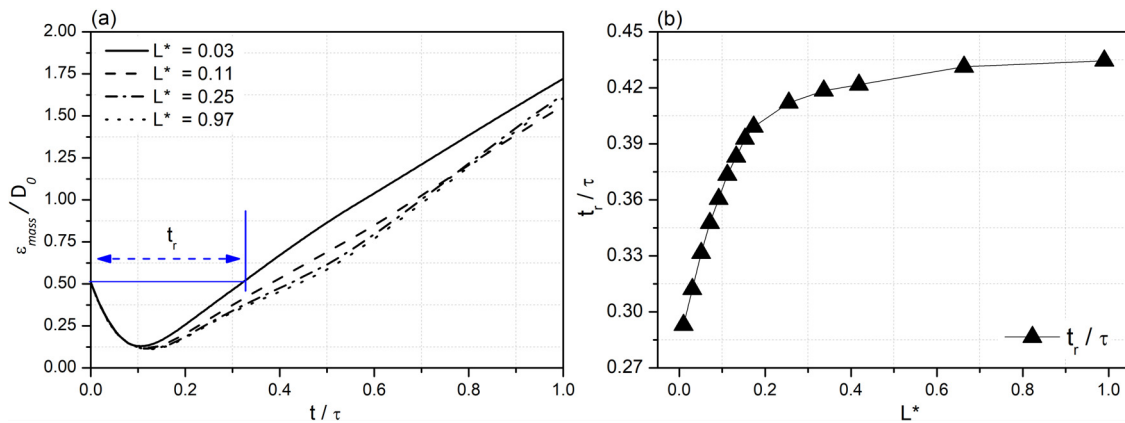


FIG. 18. (a) Transient evolution of  $\epsilon_{mass}/D_0$  and (b) normalized  $t_r$  as a function of  $L^*$  for the droplet impact on an overheated porous plate with various  $L^*$ .

with  $1 - \phi$  when  $1 - \phi > 0.1$  ( $L^* < 0.2$ ); thus, it explains why  $t_r$  is dramatically increased when  $L^* < 0.2$  [as shown in Fig. 18(b)]. Finally, we plot the dimensionless droplet rebound time  $t_r/\tau$  as a function of  $M_e/M_0$  for all cases in Fig. 20. As shown in the figure, the droplet rebound time decreases with increasing evaporation mass. In simulations of droplet impact on a porous plate, the maximum evaporation mass is higher and the minimum rebound time is smaller than the corresponding values in the flat-plate cases for the same range of Weber numbers. Remarkably,  $t_r/\tau$  can be fitted by a  $\sim (M_e/M_0)^{-0.37}$  for the cases of droplet impact on a porous plate. However, the cases of droplet impact on a flat plate clearly deviate from the power law dependency. The results for the cases of droplet impact on a porous plate demonstrate, the droplet penetration into the pores leads to a larger quantity of evaporation mass, which generates an additional lift force and accelerates the rebound of the droplet, leading to a short  $t_r$ . It should be pointed out that, in our simulations, the pore size  $D_p$  is relatively small ( $D_p/D_0 \approx 0.1$ ) and, thus, the liquid in the pores can fast evaporate. As pointed out in the above analysis, the evaporated liquid is critical to the droplet bouncing dynamics, and the droplet could

present different dynamics when the liquid in the pores evaporates to a different extent. Thus, it is necessary to extend the simulation to a wider range of surface configurations and operating parameters in future studies.

#### IV. CONCLUSION

In this study, the unified lattice Boltzmann model (ULBM) is applied to numerically investigate the droplet impact on a porous plate above the Leidenfrost temperature. The ULBM with the KBC collision operator is first validated by reproducing theoretical and experimental results of benchmark cases as well as the results of Leidenfrost droplet impingement on a flat plate. Then, we simulate the Leidenfrost droplet impingement on a plate with square pores. Effects of the droplet impacting Weber number, the plate temperature ( $Ja$ ), and the plate configuration (flat plate, porous plate, and different pore intervals  $L$ ) on droplet dynamics are revealed. The following conclusions can be drawn:

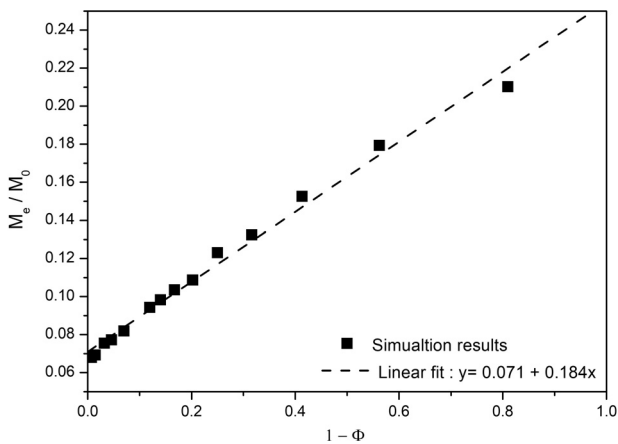


FIG. 19. Normalized droplet evaporated mass as a function  $M_e/M_0$  of surface solid fraction  $1 - \phi$ , and the dashed line in the figure represents the linear fitting function.

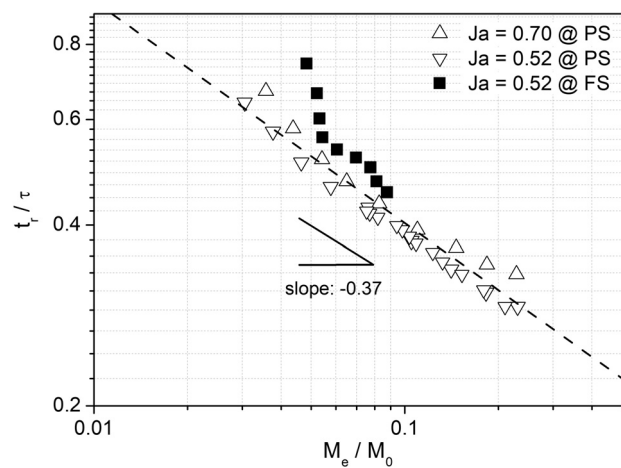


FIG. 20. Dimensionless droplet rebound time  $t_r/\tau$  as a function of normalized droplet evaporated mass  $M_e/M_0$  for all cases, and the dashed line in the figure represents the power law fitting function.



- (1) In cases with small Weber numbers, the Leidenfrost droplet impact on a porous plate shows similar bouncing morphologies as it impinges on a flat plate. On the other hand, in cases with large Weber numbers, a part of the droplet penetrates into the pores and evaporates. The vapor formed from the liquid evaporation provides additional lift force. This subsequently causes the droplet rebound in a pancake shape before its recoil, which breaks the theoretical Rayleigh's limitation and reduces the droplet contact time ( $t_c$ ) significantly.
- (2) Compared with the droplet impact on a flat plate, the droplet impact on a porous plate shows a faster rebound time ( $t_r$ ). The increase in the plate temperature and Weber number promotes the droplet rebound, and the increasing Jacob number decreases the minimum Weber number for the pancake bouncing phenomena.
- (3) The modified droplet maximum spreading time ( $t_{\max}$ ) and maximum spreading factor ( $\beta_{\max}$ ) are similar in cases with the same Weber number but various plate geometries and Jacob numbers. The evolution of  $t_{\max}/(D_{\max}^3 \rho_l / \sigma)^{0.5}$  and  $\beta_{\max}$  can be predicted by the power law functions of the Weber number in Eqs. (18) and (19), respectively. For the cases of droplet impact on a porous plate, the evaporated liquid mass linearly increases with the Weber number.
- (4) When changing the pore intervals, values of  $t_{\max}$  and  $\beta_{\max}$  keep almost unchanged and still follow the proposed power law functions [Eqs. (18) and (19)]. It is found that the droplet rebounds faster in cases with smaller normalized pore intervals  $L^*$ . In cases with the larger normalized pore intervals ( $L^* > 0.2$ ), both the droplet transient evolution and the rebound time ( $t_r$ ) are similar.
- (5) Owing to the small pore size ( $D_p/D_0 \sim 0.1$ ), the part of the droplet that is inside the pores evaporates rapidly. Therefore, the normalized droplet evaporation mass ( $M_e/M_0$ ) is proportional to the plate opening fractions ( $1-\phi$ ). The results indicate that, for the droplet impact on a porous plate, the droplet rebound time can be fitted as a power law decay function of the normalized droplet evaporation mass.

## ACKNOWLEDGMENTS

This work was supported by the UK Engineering and Physical Sciences Research Council (EPSRC) under the project "UK Consortium on Mesoscale Engineering Sciences (UKCOMES)" (Grant No. EP/R029598/1) and the project "Exascale Computing for System-Level Engineering: Design, Optimisation and Resilience" (Grant No. EP/V001531/1).

## AUTHOR DECLARATIONS

### Conflict of Interest

The authors have no conflicts to disclose.

### Author Contributions

**Geng Wang:** Conceptualization (lead); Data curation (lead); Formal analysis (lead); Investigation (lead); Methodology (lead); Software (lead); Visualization (lead); Writing – original draft (lead). **Linlin Fei:** Formal analysis (supporting); Investigation (supporting); Methodology

(supporting); Validation (supporting); Writing – review & editing (supporting). **Timan Lei:** Formal analysis (supporting); Investigation (supporting); Writing – review & editing (supporting). **Qian Wang:** Investigation (supporting); Supervision (supporting); Writing – review & editing (supporting). **Kai H. Luo:** Conceptualization (equal); Funding acquisition (lead); Supervision (lead); Writing – review & editing (equal).

## DATA AVAILABILITY

The data that support the findings of this study are available from the corresponding author upon reasonable request.

## REFERENCES

- <sup>1</sup>G. Liang and I. Mudawar, "Review of spray cooling. I. Single-phase and nucleate boiling regimes, and critical heat flux," *Int. J. Heat Mass Transfer* **115**, 1174 (2017).
- <sup>2</sup>G. Liang and I. Mudawar, "Review of spray cooling. II. High temperature boiling regimes and quenching applications," *Int. J. Heat Mass Transfer* **115**, 1206 (2017).
- <sup>3</sup>T. M. Anderson and I. Mudawar, "Microelectronic cooling by enhanced pool boiling of a dielectric fluorocarbon liquid," *J. Heat Transfer* **111**, 752 (1989).
- <sup>4</sup>D. Quéré, "Leidenfrost dynamics," *Annu. Rev. Fluid Mech.* **45**, 197 (2013).
- <sup>5</sup>V. S. Ajaev and O. A. Kabov, "Levitation and self-organization of droplets," *Annu. Rev. Fluid Mech.* **53**, 203 (2021).
- <sup>6</sup>G. Liang and I. Mudawar, "Review of drop impact on heated walls," *Int. J. Heat Mass Transfer* **106**, 103 (2017).
- <sup>7</sup>V. K. Dhir, "Boiling heat transfer," *Annu. Rev. Fluid Mech.* **30**, 365 (1998).
- <sup>8</sup>J. W. Strutt, "VI. On the capillary phenomena of jets," *Proc. R. Soc. London* **29** (196-199), 71 (1879).
- <sup>9</sup>D. Chatzikyriakou, S. P. Walker, G. F. Hewitt, C. Narayanan, and D. Lakehal, "Comparison of measured and modelled droplet-hot wall interactions," *Appl. Therm. Eng.* **29**, 1398 (2009).
- <sup>10</sup>D. Richard, C. Clanet, and D. Quéré, "Contact time of a bouncing drop," *Nature* **417**, 811 (2002).
- <sup>11</sup>Z. Hu, F. Chu, Y. Lin, and X. Wu, "Contact time of droplet impact on inclined ridged superhydrophobic surfaces," *Langmuir* **38**, 1540 (2022).
- <sup>12</sup>Z. Hu, F. Chu, and X. Wu, "Double-peak characteristic of droplet impact force on superhydrophobic surfaces," *Extreme Mech. Lett.* **52**, 101665 (2022).
- <sup>13</sup>G. Lagubeau, M. L. Merrer, C. Clanet, and D. Quéré, "Leidenfrost on a ratchet," *Nat. Phys.* **7**, 395 (2011).
- <sup>14</sup>A. Bouillant, T. Mouterde, P. Bourrianne, A. Lagarde, C. Clanet, and D. Quéré, "Leidenfrost wheels," *Nat. Phys.* **14**, 1188 (2018).
- <sup>15</sup>G. Graeber, K. Regulagadda, P. Hodel, C. Küttel, D. Landolf, T. M. Schutzius, and D. Poulikakos, "Leidenfrost droplet trampolining," *Nat. Commun.* **12**, 1727 (2021).
- <sup>16</sup>F. Celestini, T. Frisch, and Y. Pomeau, "Room temperature water Leidenfrost droplets," *Soft Matter* **9**, 9535 (2013).
- <sup>17</sup>H. M. Kwon, J. C. Bird, and K. K. Varanasi, "Increasing Leidenfrost point using micro-nano hierarchical surface structures," *Appl. Phys. Lett.* **103**, 201601 (2013).
- <sup>18</sup>C. Kruse, T. Anderson, C. Wilson, C. Zuhlke, D. Alexander, G. Gogos, and S. Ndao, "Extraordinary shifts of the Leidenfrost temperature from multiscale micro/nanostructured surfaces," *Langmuir* **29**, 9798 (2013).
- <sup>19</sup>D. Arnaldo Del Cerro, Á. G. Marín, G. R. B. E. Römer, B. Pathiraj, D. Lohse, and A. J. Huis in 't Veld, "Leidenfrost point reduction on micropatterned metallic surfaces," *Langmuir* **28**, 15106 (2012).
- <sup>20</sup>M. Jiang, Y. Wang, F. Liu, H. Du, Y. Li, H. Zhang, S. To, S. Wang, C. Pan, J. Yu, D. Quéré, and Z. Wang, "Inhibiting the Leidenfrost effect above 1000 °C for sustained thermal cooling," *Nature* **601**, 568 (2022).
- <sup>21</sup>M. Liu, H. Du, Y. Cheng, H. Zheng, Y. Jin, S. To, S. Wang, and Z. Wang, "Explosive pancake bouncing on hot superhydrophilic surfaces," *ACS Appl. Mater. Interfaces* **13**, 24321 (2021).
- <sup>22</sup>X. Zhong, Y. Zhang, Y. Hou, H. Feng, and L. Sun, "Unique dynamics of water-ethanol binary droplets impacting onto a superheated surface with nanotubes," *Int. J. Heat Mass Transfer* **164**, 120571 (2021).

- <sup>23</sup>W. Tong, L. Qiu, J. Jin, L. Sun, and F. Duan, "Unique lift-off of droplet impact on high temperature nanotube surfaces," *Appl. Phys. Lett.* **111**, 091605 (2017).
- <sup>24</sup>S. Lyua, H. Tan, Y. Wakata, X. Yang, C. K. Law, D. Lohse, and C. Sun, "On explosive boiling of a multicomponent Leidenfrost drop," *Proc. Natl. Acad. Sci. U.S.A.* **118**, e2016107118 (2021).
- <sup>25</sup>S. Lyu, V. Mathai, Y. Wang, B. Sobac, P. Colinet, D. Lohse, and C. Sun, "Final fate of a Leidenfrost droplet: Explosion or takeoff," *Sci. Adv.* **5**, 1 (2019).
- <sup>26</sup>Y. Ge and L. S. Fan, "Three-dimensional simulation of impingement of a liquid droplet on a flat surface in the Leidenfrost regime," *Phys. Fluids* **17**, 027104 (2005).
- <sup>27</sup>D. J. E. Harvie and D. F. Fletcher, "A hydrodynamic and thermodynamic simulation of droplet impacts on hot surfaces. I. Theoretical model," *Int. J. Heat Mass Transfer* **44**, 2633 (2001).
- <sup>28</sup>D. J. E. Harvie and D. F. Fletcher, "A hydrodynamic and thermodynamic simulation of droplet impacts on hot surfaces. II. Validation and applications," *Int. J. Heat Mass Transfer* **44**, 2643 (2001).
- <sup>29</sup>I. Chakraborty, M. V. Chubynsky, and J. E. Sprittles, "Computational modeling of Leidenfrost drops," *J. Fluid Mech.* **936**, A12 (2022).
- <sup>30</sup>Q. Li, K. H. Luo, Q. J. Kang, Y. L. He, Q. Chen, and Q. Liu, "Lattice Boltzmann methods for multiphase flow and phase-change heat transfer," *Prog. Energy Combust. Sci.* **52**, 62 (2016).
- <sup>31</sup>C. K. Aidun and J. R. Clausen, "Lattice-Boltzmann method for complex flows," *Annu. Rev. Fluid Mech.* **42**, 439 (2010).
- <sup>32</sup>L. Chen, Q. Kang, Y. Mu, Y. L. He, and W. Q. Tao, "A critical review of the pseudopotential multiphase lattice Boltzmann model: Methods and applications," *Int. J. Heat Mass Transfer* **76**, 210 (2014).
- <sup>33</sup>H. Huang, M. C. Sukop, and X.-Y. Lu, *Multiphase Lattice Boltzmann Methods: Theory and Application* (John Wiley and Sons, Ltd., Chichester, UK, 2015).
- <sup>34</sup>Q. Li, Q. J. Kang, M. M. Francois, and A. J. Hu, "Lattice Boltzmann modeling of self-propelled Leidenfrost droplets on ratchet surfaces," *Soft Matter* **12**, 302 (2016).
- <sup>35</sup>Z. Xu, J. Li, Z. Yao, and J. Li, "Effects of superheat degree and wettability on droplet evaporation time near Leidenfrost point through lattice Boltzmann simulation," *Int. J. Therm. Sci.* **167**, 107017 (2021).
- <sup>36</sup>N. Karami, M. H. Rahimian, and M. Farhadzadeh, "Numerical simulation of droplet evaporation on a hot surface near Leidenfrost regime using multiphase lattice Boltzmann method," *Appl. Math. Comput.* **312**, 91 (2017).
- <sup>37</sup>Y. Xu, L. Tian, C. Zhu, and N. Zhao, "Numerical investigation of droplet impact on heated surfaces with pillars," *Phys. Fluids* **34**, 023305 (2022).
- <sup>38</sup>L. Fei, J. Yang, Y. Chen, H. Mo, and K. H. Luo, "Mesoscopic simulation of three-dimensional pool boiling based on a phase-change cascaded lattice Boltzmann method," *Phys. Fluids* **32**, 103312 (2020).
- <sup>39</sup>G. Wang, L. Fei, and K. H. Luo, "Unified lattice Boltzmann method with improved schemes for multiphase flow simulation: Application to droplet dynamics under realistic conditions," *Phys. Rev. E* **105**, 045314 (2022).
- <sup>40</sup>L. Fei, K. H. Luo, and Q. Li, "Three-dimensional cascaded lattice Boltzmann method: Improved implementation and consistent forcing scheme," *Phys. Rev. E* **97**, 053309 (2018).
- <sup>41</sup>K. H. Luo, L. Fei, and G. Wang, "A unified lattice Boltzmann model and application to multiphase flows," *Philos. Trans. R. Soc. A* **379**, 20200397 (2021).
- <sup>42</sup>L. Fei, J. Du, K. H. Luo, S. Succi, M. Lauricella, A. Montessori, and Q. Wang, "Modeling realistic multiphase flows using a non-orthogonal multiple-relaxation-time lattice Boltzmann method," *Phys. Fluids* **31**, 042105 (2019).
- <sup>43</sup>I. V. Karlin, F. Bösch, and S. S. Chikatamarla, "Gibbs' principle for the lattice-kinetic theory of fluid dynamics," *Phys. Rev. E* **90**(3), 031302 (2014).
- <sup>44</sup>A. L. Kupershtokh, D. A. Medvedev, and D. I. Karpov, "On equations of state in a lattice Boltzmann method," *Comput. Math. Appl.* **58**, 965 (2009).
- <sup>45</sup>P. Yuan and L. Schaefer, "Equations of state in a lattice Boltzmann model," *Phys. Fluids* **18**, 042101 (2006).
- <sup>46</sup>Q. Li, Y. Yu, and K. H. Luo, "Implementation of contact angles in pseudopotential lattice Boltzmann simulations with curved boundaries," *Phys. Rev. E* **100**(5), 053313 (2019).
- <sup>47</sup>Q. Li, Q. J. Kang, M. M. Francois, Y. L. He, and K. H. Luo, "Lattice Boltzmann modeling of boiling heat transfer: The boiling curve and the effects of wettability," *Int. J. Heat Mass Transfer* **85**, 787–796 (2015).
- <sup>48</sup>D. Soto, H. L. Girard, A. L. Hellico, T. Binder, D. Quéré, and K. K. Varanasi, "Droplet fragmentation using a mesh," *Phys. Rev. Fluids* **3**(8), 083602 (2018).
- <sup>49</sup>G. Liang, S. Shen, Y. Guo, and J. Zhang, "Boiling from liquid drops impact on a heated wall," *Int. J. Heat Mass Transfer* **100**, 48 (2016).
- <sup>50</sup>L. H. J. Wachters, L. Smulders, J. R. Vermeulen, and H. C. Kleiweg, "The heat transfer from a hot wall to impinging mist droplets in the spheroidal state," *Chem. Eng. Sci.* **21**, 1231 (1966).
- <sup>51</sup>A. L. Biance, F. Chevy, C. Clanet, G. Lagubeau, and D. Quéré, "On the elasticity of an inertial liquid shock," *J. Fluid Mech.* **554**, 47 (2006).
- <sup>52</sup>T. Tran, H. J. J. Staat, A. Susarrey-Arce, T. C. Foertsch, A. Van Houselt, H. J. G. E. Gardeniers, A. Prosperetti, D. Lohse, and C. Sun, "Droplet impact on superheated micro-structured surfaces," *Soft Matter* **9**, 3272 (2013).
- <sup>53</sup>M. Kunihide and M. Itaru, "The behavior of a water droplet on heated surfaces," *Int. J. Heat Mass Transfer* **27**, 781 (1984).
- <sup>54</sup>G. Riboux and J. M. Gordillo, "Maximum drop radius and critical Weber number for splashing in the dynamical Leidenfrost regime," *J. Fluid Mech.* **803**, 516 (2016).
- <sup>55</sup>J. B. Lee, N. Laan, K. G. De Bruin, G. Skantzaris, N. Shahidzadeh, D. Derome, J. Carmeliet, and D. Bonn, "Universal rescaling of drop impact on smooth and rough surfaces," *J. Fluid Mech.* **786**, R41 (2015).
- <sup>56</sup>W. Yuan, T. Wei, and M. Zhang, "Dynamical vapour pocket of an impacting Leidenfrost droplet: Evaporation and scaling relations," *Int. J. Heat Fluid Flow* **95**, 108965 (2022).
- <sup>57</sup>T. Tran, H. J. J. Staat, A. Prosperetti, C. Sun, and D. Lohse, "Drop impact on superheated surfaces," *Phys. Rev. Lett.* **108**(3), 036101 (2012).
- <sup>58</sup>R. Hatakenaka, J. Breitenbach, I. V. Roisman, C. Tropea, and Y. Tagawa, "Magic carpet breakup of a drop impacting onto a heated surface in a depressurized environment," *Int. J. Heat Mass Transfer* **145**, 118729 (2019).
- <sup>59</sup>S. C. Park, M. H. Kim, S. Wongwises, D. I. Yu, and H. S. Ahn, "Explosive lift-off triggering mechanism on a surface with micropillar arrays: Liquid-vapor interface behavior between micropillars during drop impingement," *Appl. Therm. Eng.* **201**, 117739 (2022).
- <sup>60</sup>C. Te Huang, C. W. Lo, and M. C. Lu, "Reducing contact time of droplets impacting superheated hydrophobic surfaces," *Small* **18**, 2106704 (2022).
- <sup>61</sup>L. Rueda Villegas, S. Tanguy, G. Castanet, O. Caballina, and F. Lemoine, "Direct numerical simulation of the impact of a droplet onto a hot surface above the Leidenfrost temperature," *Int. J. Heat Mass Transfer* **104**, 1090 (2017).
- <sup>62</sup>G. Wang, J. Gao, and K. H. Luo, "Droplet impacting a superhydrophobic mesh array: Effect of liquid properties," *Phys. Rev. Fluids* **5**, 123605 (2020).
- <sup>63</sup>Y. Liu, L. Moevius, X. Xu, T. Qian, J. M. Yeomans, and Z. Wang, "Pancake bouncing on superhydrophobic surfaces," *Nat. Phys.* **10**, 515 (2014).
- <sup>64</sup>Z. Hu, F. Chu, and X. Wu, "Design principle of ridge-textured superhydrophobic surfaces for inducing pancake bouncing," *Int. Commun. Heat Mass Transfer* **136**, 106167 (2022).
- <sup>65</sup>J. Song, M. Gao, C. Zhao, Y. Lu, L. Huang, X. Liu, C. J. Carmalt, X. Deng, and I. P. Parkin, "Large-area fabrication of droplet pancake bouncing surface and control of bouncing state," *ACS Nano* **11**, 9259 (2017).
- <sup>66</sup>A. Mazloomi Moqaddam, S. S. Chikatamarla, and I. V. Karlin, "Drops bouncing off macro-textured superhydrophobic surfaces," *J. Fluid Mech.* **824**, 866 (2017).
- <sup>67</sup>S. Lin, B. Zhao, S. Zou, J. Guo, Z. Wei, and L. Chen, "Impact of viscous droplets on different wettable surfaces: Impact phenomena, the maximum spreading factor, spreading time and post-impact oscillation," *J. Colloid Interface Sci.* **516**, 86 (2018).
- <sup>68</sup>C. Clanet, C. Béguin, D. Richard, and D. Quéré, "Maximal deformation of an impacting drop," *J. Fluid Mech.* **517**, 199 (2004).